

High speed trot-running: Implementation of a hierarchical controller using proprioceptive impedance control on the MIT Cheetah

Dong Jin Hyun, Sangok Seok, Jongwoo Lee and Sangbae Kim

Abstract

This paper presents implementation of a highly dynamic running gait with a hierarchical controller on the MIT Cheetah. The developed controller enables high-speed running of up to 6 m/s (Froude number of $Fr \approx 7.34$) incorporating proprioceptive feedback and programmable virtual leg compliance of the MIT Cheetah. To achieve a stable and fast trot gait, we applied three control strategies: (a) programmable virtual leg compliance that provides instantaneous reflexes to external disturbance and facilitates the self-stabilizing shown in the passive dynamics of locomotion; (b) tunable stance-trajectory design, intended to adjust impulse at each foot-end in the stance phase in a high speed trot-running according to the equilibrium-point hypothesis; and (c) a gait-pattern modulation that imposes a desired cyclic gait-pattern taking cues from proprioceptive TD feedback. Based on three strategies, the controller is hierarchically structured. The control parameters for forward speeds, a specific gait-pattern, and desired leg trajectories are managed by a high-level controller. It consists of both a gait-pattern modulator with proprioceptive leg TD detection and a leg-trajectory generator using a Bézier curve and a tunable amplitude sinusoidal wave. Instead of employing physical spring/dampers in the robot's leg, the programmable virtual leg compliance is realized using proprioceptive impedance control in individual low-level leg controllers.

To verify the developed controller, a robot dynamic simulator is constructed based on the model parameters of the MIT Cheetah. The controller parameters are tuned with the simulator to achieve self-stability, and then applied to the MIT Cheetah in an experimental environment. Using leg kinematics and applied motor current feedbacks, the MIT Cheetah achieved a stable trot-running gait in the sagittal plane.

Keywords

Bioinspired legged machine, quadrupedal running, gait-pattern modulator, leg-trajectory generator, impedance control

1. Introduction

Legged machines have the potential to exceed the mobility of wheeled vehicles in rough terrain due to their inherent ability to choose situation-specific, discrete footfalls (Bares and Whittaker, 1993). This significant benefit of legged locomotion has motivated roboticists to develop legged platforms for a variety of tasks including transportation of goods (Raibert et al., 2008), exploration of hinterland, and search-and-rescue.

Many of the endeavors of robotic researchers have resulted in successful walking performances of robots using ZMP-based controllers (Yoneda et al., 1994), optimal motion-planning algorithms with machine learning (Kolter et al., 2008; Kalakrishnan et al., 2011; Shkolnik et al., 2011) even in rough terrain. However, developing a controller for fast dynamic legged locomotion remains challenging because of the requirement to robustly handle complex, nonlinear, and fast interactive dynamics between

a robot's multiple limbs and unpredictable environments, while at the same time stabilizing a robot's body. While many implementations of controllers have accomplished stable locomotion of quadrupedal robots, few, with the exception of Boston Dynamics's implementation, have succeeded at achieving the fast locomotion, rivaling that of animals (Boston Dynamics, 2009).

In developing a controller for achieving this challenging task, there are three primary issues to be mainly considered: (a) stability criteria in locomotion, (b) modulation of gait-pattern, and (c) control of ground reaction force.

Department of Mechanical Engineering, MIT, Cambridge, MA, USA

Corresponding author:

Dong Jin Hyun, Department of Mechanical Engineering, MIT, Cambridge, MA 02139, USA.
Email: mecjin@gmail.com

1.1. Three primary issues with previous research

1.1.1. Stability criteria in locomotion. Stability criteria in legged locomotion are not clearly defined despite several studies on legged dynamics (McGhee and Frank, 1968; Full et al., 2002; Altendorfer et al., 2004). Due to the absence of comprehensive methods to quantify stability, the design of stabilizing controllers using numerical optimization methods for fast locomotion is challenging. Furthermore, many previous controllers were heavily dependent on the sensory feedback of the robot's global states, such as the robot's body pitch and forward velocity for stability, and its force exertion on the ground (Estremera and Waldron, 2008; Krasny and Orin, 2010; Gehring et al., 2013). However, the implementation of these controllers in autonomous systems is hindered by the lack of robust autonomous global body state measurement technologies for highly dynamic running.

Therefore, the existence of the self-stabilizing¹ in high-speed locomotion has been extensively investigated by employing the passive dynamics of springy legs inspired by biological observations (Full and Koditschek, 1999). The Spring Loaded Inverted Pendulum (SLIP) model has been especially effective in the study of locomotive stability due to its simplicity and conformity to biological observation since Blickhan (1989) proposed a simple spring-mass model to describe the legged dynamics observed in running animals. With the SLIP model, Ghigliazza et al. (2003) pointed out that stable periodic cycles of passive dynamics exist for some initial states in a certain range of leg stiffness. Ringrose (1997) implemented this self-stabilizing running with a monopod robot, and the iSprawl achieved fast hexapedal locomotion preserving self-stabilizing dynamics (Kim et al., 2006). Furthermore, it was revealed that proper active hip actuation enlarges the stability margin for this self-stability (Seipel and Holmes, 2007).

1.1.2. Modulation of gait-pattern. Modulating gait-pattern—controlling the sequence of the footfalls—is a critical part of legged locomotion. For quadrupedal running, in particular, the coordination of four limbs at various speeds plays a critical role in locomotive performance. Biological observation has been a great source for understanding the principles of animals' gait-patterns. Temporal/spatial analyses on animal gaits have revealed the various relationships among stride frequency, stride length, and speed of locomotion (Vilensky et al., 1991; Wickler et al., 2003; Maes et al., 2008). These studies have revealed a few interesting trends. First, animals tend to use a specific gait for a given speed. Second, the strategy animals use to increase locomotion speed depends on the gait-pattern; for a trot, they increase stride frequency, whereas for a gallop they increase stride length. Different roles for each leg in a galloping gait-pattern were also investigated based on ground reaction force analysis of a galloping dog (Lee et al., 1999; Walter and Carrier, 2006).

To realize animals' gait-patterns inspired from the neural circuits discovered in animals, various types of Central Pattern Generators (CPGs) have been proposed (Grillner and Wallen, 1985; Ijspeert, 2008). These CPGs resemble animals' motor pattern production, producing the oscillators that create rhythmic signal outputs. However, lack of sensory feedback might lead to absence of the adaptability to the environment and instability of locomotion. Therefore, the Kotetsu (Maufroy et al., 2010) and the Tekken (Fukuoka et al., 2003) included external feedback to provide adaptability to environment by modulating the output signals of an oscillator. While employing CPGs successfully generates the desired pattern in many robots with a wide stance, which is mostly statically stable, it is still difficult to understand how animals such as cheetahs, whose stance is very narrow, coordinate CPGs with extero/proprioceptive sensory feedback to secure dynamic stability. In order to develop a controller that enables high-speed agile robots, it is important to learn how to enhance dynamic stability, combining the pattern generation with sensory feedback.

1.1.3. Modulation of ground reaction force. Within a given gait-pattern, for high-speed running, it is important to control the ground reaction force (GRF) at each foot in order to keep the body posture in a desired periodic pattern. This is an example of an intuitive approach to improve the stability of the overall locomotion dynamics. Although well-tuned impedance control can enable self-stabilized behaviors in symmetric gaits, in order to enhance robustness it is desirable to add feedback control to modulate the ground reaction forces. Especially for high-speed quadruped running, a gallop gait seems more desirable for an animal, and the application of the SLIP model is limited since the gallop is an asymmetric gait and employs a range of gait-patterns. For a force-control approach, Koepf et al. (2010) and Koepf and Hurst (2011) proposed that a well-defined force profile to satisfy momentum conservation for running can be used to control vertical bouncing. However, the implementation of a desired force profile within a short stance time (60 ms stance period at 6 m/s running according to our experimental results) for a robot's high-speed running is challenging, especially including the synchronization of the force command with the leg TD event.

Instead of directly implementing force control, the compliance-force control can be used to exert forces at foot-ends in the stance phase by controlling the equilibrium position of the impedance control. Bizzi et al. (1992) observed that an equilibrium position of the springy muscular system is specified by the neural activity for limb motion control, and proposed the *Equilibrium-point hypothesis* such that the contact force control can be effectively accomplished as well by penetrating the equilibrium position of the impedance control into the surface. Hogan (1987) demonstrated this approach in a grounded manipulator interacting with a wall. If the desired force profile is generated with respect to the inertial coordinate, both

approaches must have accurate global attitude measurement of the robot because the directions of the force have to be controlled.

1.2. Approach and paper outline.

We consider solutions to these three issues critical constituents of the successful design of a controller that enables stable, versatile, and efficient locomotion. Even though these critical issues are intricately interconnected, they can be handled with three separate strategies.

To effectively address these three issues in high-speed locomotion and implement characteristics of biological quadrupedal gaits, we developed a hierarchical control architecture consisting of three components: (a) a leg controller to realize the virtual leg compliance by using the impedance control as a low-level controller; (b) a gait-pattern modulator to impose an intended gait-pattern on a leg-trajectory generator as one high-level controller; and (c) a leg-trajectory generator to provide a designed foot-end trajectory for a leg controller as the other high-level controller.

First, we developed a low-level leg controller that creates programmable compliance through proprioceptive force control actuators (Seok et al., 2012), in order to facilitate the self-stability of the locomotion, employing the impedance force control (Hogan, 1985). This programmable virtual leg compliance provides reflex responses to external forces. Similar strategies relying on this self-stability have been suggested previously (Geyer et al., 2002; Blickhan et al., 2007), but common approaches to realizing desired compliance require installation of mechanical springs and dampers in a robot's leg (Poulakakis et al., 2006; Cotton et al., 2012; Spröwitz et al., 2013). These mechanical solutions, though, lead to deterioration of force-control performance, challenges in tuning leg compliance, and inefficiency in locomotion. Programmable virtual leg compliance overcomes these drawbacks when successfully implemented in high bandwidth (4 kHz) to realize a desired leg impedance on demand. Then, the coordination of these four compliant virtual legs with the desired forward speed is determined by the gait-pattern modulator.

Second, our controller architecture successfully combines our gait-pattern modulator with a leg's proprioceptive TD detection as a sensory feedback. The combination effectively manages the coordination of four legs by tying the time phases of three legs to the reference leg. The time phase of the reference leg is activated by the leg's TD event detection for "stride-to-stride" gait-pattern adaptation to the environment. Similarly, Righetti and Ijspeert (2008) used the output signals of a CPG, based on each leg's independent TD sensory feedback from an external foot-force sensor. However, our gait-pattern modulator has two distinguishing features. First, the reference leg's TD is detected by the proprioceptive force-control actuator without any additional force sensor and the desired gait-pattern

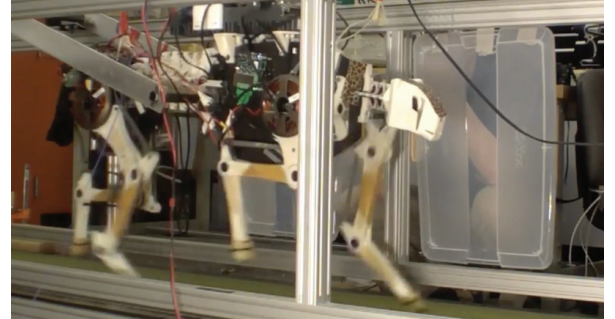


Fig. 1. The running MIT Cheetah on the treadmill up to 6 m/s with trot gait, while constrained in its sagittal plane. It has 12 DoF; 1 DoF for ab/adduction and 2 DoF for both shoulder/hip and knee motion for the four legs.

is defined by other legs' phase differences with respect to the TD event of this reference leg in one stride. Second, while multiple CPG-based robots directly relate the pattern signals to desired joint trajectories for each joint position controller, the proposed gait-pattern modulator only determines temporal gait characteristics such as forward velocity and time-phase differences between the legs. The spatial characteristics, such as hip height, angle of attack, swing-leg retraction, step length, and stance trajectories for contact-force control, are independently handled in the leg-trajectory generator as the other part of the high-level controller.

The third characteristic in our control architecture is the leg-trajectory generator to match the pattern signals from the gait-pattern modulator to each foot-end position as an instant equilibrium point of the impedance control. A pre-defined sinusoidal GRF at each leg resulted in the self-stabilizing hexapod running at a preferred forward velocity (Kubow and Full, 1999). Similarly, the stance-phase trajectory is constructed by a sinusoidal wave with an adjustable amplitude to modulate vertical impulse (time integral of vertical GRF). Through a developed simulator and an experiment, this amplitude of the sinusoidal stance trajectory is tuned to achieve stability in locomotion. The swing-phase trajectory is designed using properties of the Bézier curve for desirable swing-leg dynamics. These two trajectories have identical but tunable stroke length to maintain continuity at the transition between swing/stance phases. Furthermore, considering the derivative of the Bézier curve, the foot speed in the swing-leg retraction is adjustable to reduce the TD energy losses of running (Haberland et al., 2011).

Three strategies are integrated hierarchically in the proposed controller to tackle three issues, and the controller was implemented on the MIT Cheetah after validation using the developed simulator. It was capable of variable-speed trot-running with little pitch/height variation as shown in Figure 1. The robot recorded the maximum speed limited by the speed of a treadmill, 6 m/s, which corresponds to a Froude number (Fr) of 7.34. The Fr is one of indices

used to compare dynamic locomotion because, whenever similar characteristics are observed among different-sized quadrupeds, their corresponding Fr are similar (Alexander, 1984). Since the beginning of the development of legged machines, to the best of the authors' knowledge, a robot in a robotic research community has rarely been able to run with an Fr higher than 1. Only the pioneering work of Raibert ($Fr = 1.53$) in 1990 and the Cheetah-cub of the EPFL ($Fr = 1.30$) in 2013 achieved an Fr higher than 1 (Spröwitz et al., 2013).

In addition to achieving the stable trot-running, the gait transition from trot to gallop was tried at 6 m/s. Through this test, we intended to test the gait-transition capability of the controller and to prepare for the robot's galloping experiment as our future work. This "trot-to-gallop" experiment shows the smooth change of leg coordination in a desired time duration.

This paper is structured as follows: Section 2 presents the mathematics and algorithms to construct a simulator of the MIT Cheetah. In Section 3, the control framework is explained in detail. The validity of the proposed controller is verified with simulation in Section 4. Experimental results with the proposed controller on the MIT Cheetah are provided and discussed in Sections 5 and 6. Lastly, conclusions and open research topics are addressed in Section 7.

2. Modeling of the MIT Cheetah

A simulator was developed using MATLAB to verify the self-stabilizing in locomotion with the proposed controller, and validate the controller's tunable parameters, such as control gains for virtual leg compliance², control points for leg-trajectory and force-interaction with the ground. Unconstrained equations of motion of the MIT Cheetah were derived using Lagrangian formulation, and additional holonomic constraints were applied to obtain stance dynamics of the robot. The robot and its planar rigid body model are depicted in Figure 2 with generalized coordinates and leg index $i \in \{FL, FR, BL, BR\}$. Each segment of the robot is assumed to be rigid and connected to each other via frictionless revolute joints. The inertial and geometrical properties such as masses, moments of inertia, center of mass positions, and segment lengths are obtained from Solidworks's design of the MIT Cheetah. Model parameter values are listed in Table 6 in Appendix Appendix B.

The robot model has 11 degrees of freedom (DoF). The proximal and distal segments of each leg are parallel according to the pantographic leg design, so that the configuration of a three-segmented-leg can be determined by two joint coordinates. Three independent coordinates (x, y, q_{pitch}) define the body position and posture with respect to the inertial reference frame. A flexible spine which consists of four urethane rubber joints is designed to be dependent on the hip angles of both hind legs ($q_{1,BR}, q_{1,BL}$) by coupling the motion of the hind legs to

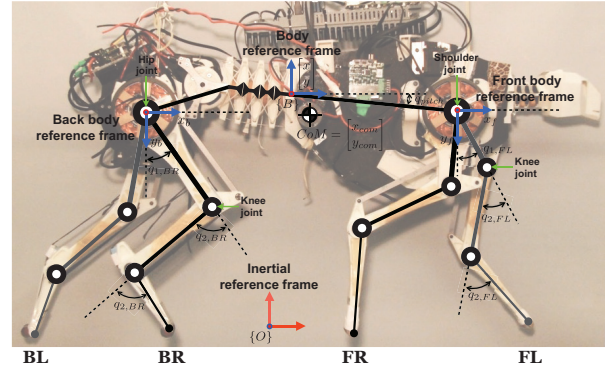


Fig. 2. The planar-rigid model of the MIT Cheetah on the rigid flat ground. Leg indices are also listed; FR: front and right side, FL: front and left side, BR: back and right side, and BL: back and left side.

the spine using a cable-driven differential gear mechanism: when motion of the hind legs are in-phase, the spine is actuated and otherwise it remains near a neutral position. Therefore, the motion of the spine can be described by hip angles of the hind legs. The nonlinear compliance of the spine was not able to be accurately measured and disregarded in this modeling. The effect of the model discrepancy due to the flexible spine, however, is expected to be insignificant with the trot gait since motion of hind legs during trot gaits are mostly out-of-phase. The kinematic relation between each joint of the spine and hip joints of the hind legs is measured from the MIT Cheetah in Appendix Appendix C.

The interaction between the robot and the ground is modeled as follows: the ground is modeled as a rigid half-space, and the legs of the robot are assumed to interact with the ground as point feet. Impulsive/non-impulsive interaction forces follow the Coulomb friction model. For the sake of simplicity, we assume that friction coefficient (μ) is constant, and its value is 1.0, considering interaction between the MIT Cheetah's rubber foot and a treadmill (Baraff, 1991). Collision of the point-foot and the ground is modeled to be perfectly inelastic in the normal direction.

2.1. Constrained equations of motion (EoM)

Equations of motion for the 11-DoF MIT Cheetah is described by

$$D(q)\ddot{q} + C(q, \dot{q})\dot{q} + G(q) = B(q)u + J_c(q)^T F_{\text{ext}} \quad (1)$$

where $q := [q_{\text{pitch}}, q_{1,FR}, q_{2,FR}, \dots, q_{1,BL}, q_{2,BL}, x, y] \in \mathbb{R}^{11}$ is the generalized coordinates of the model. $D(q)$, $C(q, \dot{q})\dot{q}$, $G(q)$, and $B(q)$ are the inertial matrix, Coriolis and centrifugal terms, gravitational torque vector, and the input matrix, respectively. $u \in \mathbb{R}^8$ is a vector of torque outputs at each joint from BLDC motors through actuation transmission. $J_c(q) = \frac{\partial p_c(q)}{\partial q}$ is a Jacobian matrix of $p_c(q) \in \mathbb{R}^{2N_c \times 1}$, a stack of position vectors of each ground-contact foot with respect to the inertial frame. N_c is the number of

ground-contact feet. $J_c(q)^T F_{\text{ext}}$ is the GRFs represented in the joint space.

To solve for \ddot{q} and F_{ext} , holonomic equality constraints on the positions of the ground-contact legs have to be considered:

$$\Phi(q) = 0_{h \times 1} \quad \dot{\Phi}(q) = 0_{h \times 1} \quad (2)$$

where h is the number of constraints. The equality constraint for each leg is applied from the moment when the leg makes contact with the ground. To inhibit violation of the constraints due to the accumulation of numerical drift, the Baumgarte's stabilization method (Baumgarte, 1972) is introduced into the dynamics solver:

$$\ddot{\Phi}(q) + 2\alpha \dot{\Phi}(q) + \beta^2 \Phi(q) = 0 \quad (3)$$

where α and β are called Baumgarte parameters. Therefore, two bundles of equations, equations (1) and (3), are solved simultaneously to compute \ddot{q} and F_{ext} at each time step (Witkin et al., 1990) by

$$\begin{bmatrix} D(q) - J_c^T(q) \\ J_c(q) \end{bmatrix} \begin{bmatrix} \ddot{q} \\ F_{\text{ext}} \end{bmatrix} = \begin{bmatrix} -C(q, \dot{q})\dot{q} - G(q) + B(q)u \\ -J_c(q)\dot{q} - 2\alpha\dot{\Phi} - \beta^2\Phi \end{bmatrix} \quad (4)$$

2.2. Impact map

When legs' touch-down (TD) events happen, the system states undergo an abrupt change due to large impulsive forces during a short period time of impact. The generalized velocities after impact, \dot{q}^+ , can be solved via the algebraic impact law, equation (6), with appropriate equality constraints, equation (7), based on the method introduced in Hurmuzlu et al. (1994).

$$\dot{q}^+ = \dot{q}^- \quad (5)$$

$$D(q)\dot{q}^+ - D(q)\dot{q}^- = J_c(q)^T \int F_{\text{ext}} dt \quad (6)$$

$$\dot{\Phi}(q) = 0_{h \times 1} \quad (7)$$

Having the updated system states, \dot{q}^+ and \dot{q}^+ , and the updated constraint equations, the interactive dynamics between the robot and the ground are then simulated with the Coulomb friction model.

2.3. The Coulomb friction model

Due to lack of the accurate ground model, it is challenging to design a controller to prevent a robot from slipping at every step. Therefore, allowing slip in the simulator environment with an appropriate friction model provides a more realistic way of assessing robustness of a designed controller.

The Coulomb friction model defines a relation between tangential and normal components of the GRF, F_t and F_n respectively, namely the friction cone: $|F_t| \leq \mu|F_n|$. Here μ is the friction coefficient between a foot and the

ground. Computed GRFs, F_{ext} , from equations (1) and (3) should obey the friction cone, and are closely related to the construction of equality constraints, equation (2).

The equality constraints are applied to the positions of each ground-contact foot. We classify a “non-slip ground-contact foot” (NS) and a “slip ground-contact foot” (S) and assign equality constraints accordingly.

$$\Phi(q) = \begin{bmatrix} p_c^{NS}(q) \\ p_{c,n}^S(q) \end{bmatrix} - \begin{bmatrix} p_c^{NS}(q_0) \\ p_{c,n}^S(q_0) \end{bmatrix} = \begin{bmatrix} 0_{2N_{NS} \times 1} \\ 0_{N_S \times 1} \end{bmatrix} \quad (8)$$

$$\dot{\Phi}(q) = \frac{\partial}{\partial q} \begin{bmatrix} p_c^{NS}(q) \\ p_{c,n}^S(q) \end{bmatrix} \dot{q} = \begin{bmatrix} J^{NS}(q) \\ J_n^S(q) \end{bmatrix} \dot{q} = \begin{bmatrix} 0_{2N_{NS} \times 1} \\ 0_{N_S \times 1} \end{bmatrix} \quad (9)$$

where q_0 is the generalized coordinates at the TD event. An NS position should be fixed during integration, whereas the constraint in the tangential direction for an S position should be eliminated in order to allow it to accelerate along the tangential direction. N_{NS} is the number of NS, and N_S is the number of S.

If the foot slips the magnitude of the tangential component of GRF is limited by the friction cone ($|F_t^S| = \mu|F_n^S|$). Hence, the $J_c^T F_{\text{ext}}$ term in the equation (1) is constructed as follows to reduce the number of unknown variables: from \ddot{q} and $F_{\text{ext}} = [F_t^{NS}, F_n^{NS}, F_t^S, F_n^S]^T$ to \ddot{q} and $F_{\text{ext}} = [F_t^{NS}, F_n^{NS}, F_n^S]^T$.

$$J_c^T F_{\text{ext}} = \begin{bmatrix} J^{NS} \\ J_n^S + M J_t^S \end{bmatrix}^T F_{\text{ext}} \quad (10)$$

where M is a diagonal matrix of μ with slip direction information. The impact map considering the Coulomb friction model is constructed in a similar manner (Lee, 2013).

The multi-Dof planar rigid body model of the robot with the impact map and the Coulomb friction model is utilized to validate the performance of a control framework proposed in the following section. In Section 4, we present properly chosen parameters of the proposed controller and corresponding simulation results.

3. Quadrupedal locomotive control framework

This section addresses a locomotive control framework for quadrupedal robots, which is based on two hypotheses:

1. The robot's self-stabilizing behavior in locomotion, without active stabilization efforts, can be preserved by appropriately programming the virtual leg compliance.
2. According to the *equilibrium-point hypothesis*, the modulation of ground impulse is feasible through design of the foot-end trajectories for the stance phase.

The primary objective of the proposed framework is to describe quadrupedal locomotion with minimized number of control parameters such as forward speed, gait-patterns, and foot-end trajectories. The overall structure of the proposed controller is schematically represented in Figure 3.

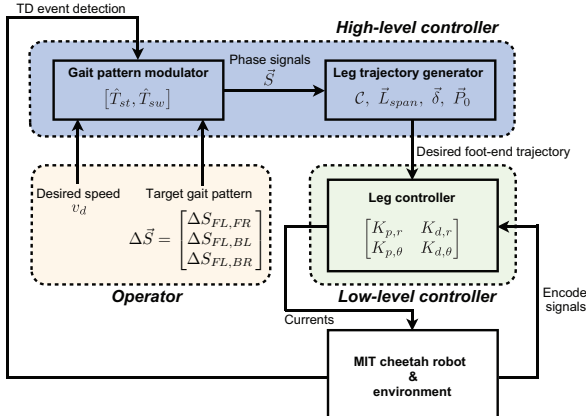


Fig. 3. Schematic overall structure of the proposed hierarchical locomotive control framework. Each block represents one stage and its corresponding control parameters. In this schematic diagram, the *reference leg* is the front left leg, FL.

Table 1. Nomenclature for control parameters.

Terminology	Definition
v_d	Desired speed
$\Delta S_{FL,i}$	The phase lag between FL leg and leg i
\hat{T}_{st}	Desired stance phase period
\hat{T}_{sw}	Desired swing phase period
$C = [C_F, C_B]$	Bezier control points for swing phase trajectory
$\vec{L}_{\text{span}} = (L_{\text{span},F}, L_{\text{span},B})^T$	Half of the stroke length
$\delta = (\delta_F, \delta_B)^T$	Penetration depth for stance phase trajectory
$\vec{P}_0 = (P_{0,F}, P_{0,B})^T$	Reference point of the trajectory
$K_{p,r}$	Radial stiffness of each leg
$K_{d,r}$	Radial damping of each leg
$K_{p,\theta}$	Angular stiffness of each leg
$K_{d,\theta}$	Angular damping of each leg

The gait-pattern modulator and the leg-trajectory generator constitute the high-level controller which determines gait coordination among four legs and trajectories of each leg. An operator specifies (a) a desired velocity v_d and (b) a target gait-pattern expressed by ΔS . Also, the proprioceptive TD detection on the “*reference leg*” provides the controller with the stride-initiation timing. The low-level individual leg controller follows the impedance control. Table 1 shows the control variables to be managed in the proposed controller.

3.1. Gait pattern modulator with proprioceptive sensory feedback

The gait-pattern modulator achieves a desired velocity and a target gait-pattern by coordinating the robot’s four limbs with phase signals, S . The phase signal of each leg is

defined to be a timed location in the desired stride period. The desired stride period is the sum of the desired stance and the desired swing phase period, $\hat{T}_{\text{stride}} = \hat{T}_{\text{sw}} + \hat{T}_{\text{st}}$, which are determined in accordance with the commanded desired velocity.

The temporal limb coordination, a gait-pattern, is a major component that characterizes quadrupedal locomotion. To impose a specific target gait-pattern such as walk, trot, canter, and gallop, the gait-pattern modulator assigns phase lag, ΔS , among four legs.

3.1.1. Phase signals. Generated phase signals are referred as parameters by the leg-trajectory generator for purposes of designing stance/swing phase trajectories. Each signal $S_i^j \in [0, 1]$ is time-normalized by \hat{T}_{st} and \hat{T}_{sw} , where $i \in \{\text{FL, FR, BL, BR}\}$ is the leg index and $j \in \{\text{st, sw}\}$ is the leg-state index (stance, swing).

Maes et al. (2008) showed that the swing period of dogs’ running experiments remains relatively constant over a wide range of speeds. We believe that dogs try to minimize the swing phase regardless of locomotion speed and thus maximizes the ground phase. We also choose the shortest swing period that allows a decent trajectory tracking control to maximize the ground phase to improve stability and minimize the peak torque of the motor. The constant desired swing phase period, \hat{T}_{sw} , is prescribed as 0.25 s. Furthermore, identical swing dynamics of a pair of contralateral legs provides a high-level controller with a simple way to stabilize body dynamics.

In animals, while swing duration is maintained, stride frequency and contact time decrease as speed increases (Vilensky et al., 1991; Wickler et al., 2003). Therefore the desired stance phase period, \hat{T}_{st} , is determined according to the desired speed v_d as:

$$\hat{T}_{\text{st}} = \frac{2L_{\text{span}}}{v_d} \quad (11)$$

where L_{span} is half of the stroke length (as depicted in Figure 6, below), which is also a half of the approximation of distance traveled of the shoulder/hip joint during the stance phase. This implies that stride frequencies are modulated to accelerate, which is similar to Kim et al. (2006). Once the gait-pattern modulator is triggered, it assigns a stance phase S_i^{st} and then a swing phase S_i^{sw} to each leg, which completes a whole stride. If an operator increases the forward speed of the robot, the gait-pattern modulator generates sawtooth signals as shown in Figure 4 for each leg according to an increased frequency after completion of the on-going stride.

3.1.2. Synchronization by proprioceptive sensory feedback. The phase signals generated by the gait-pattern modulator have to be synchronized with the environment such that the stance phase and the swing phase is properly commanded to a leg when it touches down or lifts off the ground, respectively. Therefore, the detection of TD events and lift-off (LO) events become crucial. In many researches on legged

robots, a force sensor is attached to the foot-end for the event detection as well as for interactive force-feedback control and event-based stance-swing switching control.

The low mechanical impedance of the MIT Cheetah's leg enables the proprioceptive TD detection without additional force sensor, by sensing abrupt changes in the commanded force computed by the impedance control scheme. These changes are significant, higher than ones commanded during the swing phase. Therefore, the detection of the TD event can be analogous to a threshold switch, by setting a threshold value on radial force, F_r . This type of sensing might be vulnerable to chattering of the leg that can lead to multiple mis-detections during an on-going stance phase. Therefore, if the TD event is detected once, it is disabled until completing the full stance phase and additional 90% of the swing phase. Note that the leg's motion after executing 90% of the swing phase would be primarily under the centrifugal force in the radially outward direction. The proprioceptive TD feedback is activated by the radially inward direction force.

3.1.3. Imposing gait-patterns. In order to impose a desired gait-pattern, phase coupling among four legs is required together with synchronization of legs' TD. If all the leg-phases are initiated by each TD event, however, it is challenging to maintain the consistency of the desired gait-pattern with a constant swing period policy. Therefore, a simple, but effective way to maintain the consistency of the gait-pattern has been adopted: *TD event-based stride-to-stride pattern modulation*. Detection of a TD event at the reference leg initiates the leg's phase signal generation; the other three legs' phases are matched to that of the reference leg with designated phase lag, ΔS . The proposed method is versatile enough to define symmetric/asymmetric gait-pattern in one stride.

This "stride-to-stride" method generates phase signals for one stride and then waits for the next trigger. Therefore, after completion of one stride, all the legs become stationary until the next TD event is detected on the reference leg. This undesired stationary period is the result of minimal adaptation to the environment while maintaining a specific gait-pattern, which is necessary for locomotion on a rough terrain with unexpected external disturbances. Ideally, the undesired stationary period can be removed when the sum of two period variables for the stance/swing phase in the controller, $\hat{T}_{sw} + \hat{T}_{st}$, are well matched to the actual period.

3.1.4. Phase signal generation according to TD elapsed time and phase differences. A mathematical formulation of the described phase signals is presented here. The phase signals are created referring to the clocks of each leg in one stride. The reference leg clock is the time elapsed after a TD event, and the other clocks have time delay with respect to the reference leg clock.

The proprioceptive TD detection is represented as a boolean variable TD. It changes from FALSE to TRUE

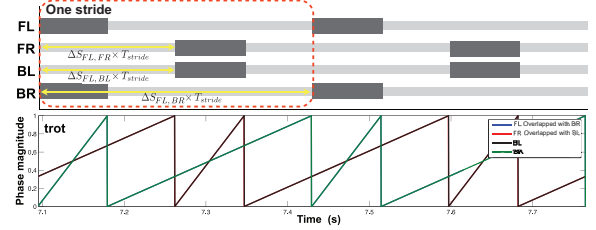


Fig. 4. Sawtooth phase signals generated by gait-pattern modulator for trot gait and its corresponding footfall-pattern diagram. The phase difference is represented in the diagram.

when the event is detected, and one stride proceeds with the elapsed time after the event as follows:

$$t_{ref}^{elapse} = \begin{cases} t - t_{ref}^{TD} & \text{if } t_{ref}^{elapse} > \hat{T}_{stride} \\ \hat{T}_{stride} & \text{if } t_{ref}^{elapse} \leq \hat{T}_{stride} \end{cases} \quad (12)$$

$$t_{ref}^{TD} = t \text{ if } (S_{ref}^{sw} > 0.9) \wedge (\text{TD}) \quad (13)$$

$$t_i = t_{ref}^{elapse} - \Delta S_{ref,i} \hat{T}_{stride} \quad (14)$$

where t_{ref}^{elapse} is the elapsed time after t_{ref}^{TD} , which is the moment of the TD event on the reference leg. t_i is the clock for each leg, where $i \in \{\text{FL}, \text{FR}, \text{BL}, \text{BR}\}$. $\Delta S_{ref,i}$ is the phase lag of the leg i with respect to the reference leg, represented as a fraction of the desired stride period. Note that $\Delta S_{ref,ref}$ is zero by definition. t_{ref}^{TD} is updated discretely when the next TD event is detected, while 90% of the swing phase of the reference leg (S_{ref}^{sw}) is completed.

S_i^{st} increases from zero to one during \hat{T}_{st} and subsequently S_i^{sw} repeats from zero to one during \hat{T}_{sw} . Each leg phase signal follows the reference time having its phase lag.

$$S_i^{st} = \frac{t_i}{\hat{T}_{st}} \quad 0 < t_i < \hat{T}_{st} \quad (15)$$

$$S_i^{sw} = \begin{cases} \frac{t_i + \hat{T}_{sw}}{\hat{T}_{sw}} & \text{if } -\hat{T}_{sw} < t_i < 0 \\ \frac{t_i - \hat{T}_{st}}{\hat{T}_{sw}} & \text{if } \hat{T}_{st} < t_i < \hat{T}_{stride} \end{cases} \quad (16)$$

Here we present the phase signals generated by the proposed gait-pattern modulator and corresponding footfall-pattern diagrams for the trot and gallop gait-patterns used for the executed experiment. The FL is chosen as the reference leg in the examples. To accomplish a specific gait-pattern, appropriate phase lags are prescribed with respect to the FL leg. The trot gait is a symmetric gait-pattern which has matching phases for contralateral legs as in Figure 4.

$$\Delta \vec{S}_{trot} = \begin{bmatrix} \Delta S_{FL,FR} \\ \Delta S_{FL,BL} \\ \Delta S_{FL,BR} \end{bmatrix}_{trot} = \begin{bmatrix} 0.5 \\ 0.5 \\ 0 \end{bmatrix} \quad (17)$$

The phase differences among four legs for a gallop in animals, which is an asymmetric gait-pattern, are observed to vary according to the speed and the types of gallop. Here,

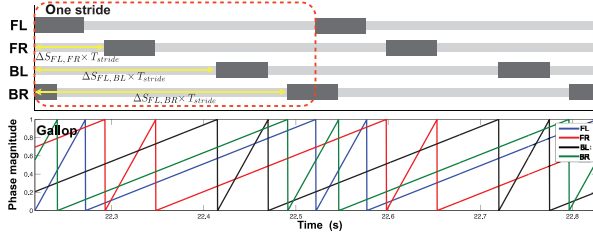


Fig. 5. Sawtooth phase signals generated by the gait-pattern modulator for gallop gait and its corresponding footfall-pattern diagram. The phase difference is represented in the diagram.

as one example, the following phase differences are chosen for the gallops in Figure 5.

$$\Delta \vec{S}_{\text{gallop}} = \begin{bmatrix} \Delta S_{\text{FL,FR}} \\ \Delta S_{\text{FL,BL}} \\ \Delta S_{\text{FL,BR}} \end{bmatrix}_{\text{gallop}} = \begin{bmatrix} 0.2 \\ 0.55 \\ 0.75 \end{bmatrix} \quad (18)$$

3.1.5. Change of gait-pattern for trot-to-gallop gait transition. For the gait transition, a simple leg coordination changing algorithm compatible with the gait-pattern modulator is also proposed. The biological principle of gait transition in animals is not fully understood, but it is both hypothesized and observed that animals have desirable gait-patterns for different speeds in terms of either metabolic energy efficiency (Wickler et al., 2003) or minimal peak forces for each limb (Farley and Taylor, 1991), and therefore gait transition is necessary while accelerating or decelerating. As a gait-pattern is defined with the phase-lag vector $\Delta \vec{S}$, a smooth and continuous change of the leg coordination can be achieved by varying $\Delta \vec{S}$ linearly with time over multiple stride times or a specified duration. For example, the leg coordination for the trot-to-gallop transition can be described as

$$\Delta \vec{S} = \Delta \vec{S}_{\text{trot}} + (\Delta \vec{S}_{\text{gallop}} - \Delta \vec{S}_{\text{trot}}) SAT \left(\frac{t - t_{\text{gt}}}{\Delta T_{\text{gt}}}, 1 \right) \quad (19)$$

where t_{gt} is the transition starting time, ΔT_{gt} is the duration of the gait transition, and SAT is the saturation function.³ This simple gait transition strategy can be effective if the robot after the leg coordination change can be stabilized with the proposed controller with a tuned set of parameters for the gallop gait.

3.2. Leg trajectory generator

The leg-trajectory generator transforms the phase signals from the gait-pattern modulator to the desired trajectories for each foot-end, which are designed with variable parameters. The leg-trajectory generator plays a key role in our scheme: the robot is capable of managing its stability with adjustable trajectories while following a specific gait-pattern commanded by the gait-pattern modulator. The

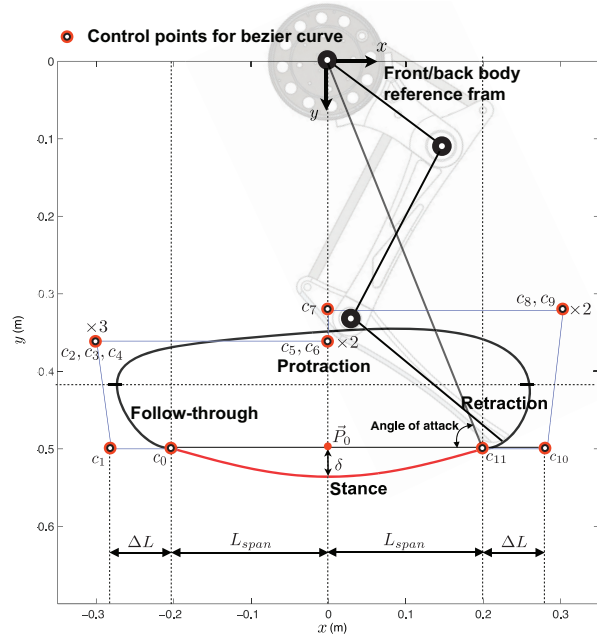


Fig. 6. A desired foot-end trajectory defined by the control parameters c_k , L_{span} , δ , and \vec{P}_0 . 12 control points of Bézier curve for the swing-phase trajectory (black solid line) are shown in the figure. Multiple overlapped points are denoted as “ $\times n$ ”. The sinusoidal wave of the stance-phase trajectory is shown together (red solid line).

swing-phase and the stance-phase trajectories are designed individually for different purposes; the position-control and the compliance-force control.

The swing-phase trajectories are designed from a Bézier curve defined by a set of 12 control points, $\mathcal{C} = \{c_k\}$, and stance-phase trajectories are spatially designed as sinusoidal waves of which the period is twice the stroke length. Also, both trajectories are designed around a single reference point, \vec{P}_0 with respect to the local shoulder/hip coordinate system. Figure 6 shows the designed reference gait trajectory.

3.2.1. Design of the trajectory in the swing phase. The primary design objective of the swing-phase trajectory is to protract a leg with sufficient ground clearance in order to avoid obstacles, and to have desirable swing leg retraction rate in order to reduce TD energy losses of running (Haberland et al., 2011). Also, a well designed smooth swing-phase trajectory in the feasible leg-workspace, $p_i^{\text{sw}}(t)$, prevents abrupt changes in leg dynamics like jerk which can lead to the instability of the whole body.

The three-segmented pantographic design of the MIT Cheetah leg enables protraction with low energy usage by exploiting its natural dynamics. A swing phase trajectory is designed by a two-dimensional Bézier curve constructed with 12 control points. This design approximates the protraction trajectory to around the natural behavior of the legs, as well as satisfying geometrical requirements

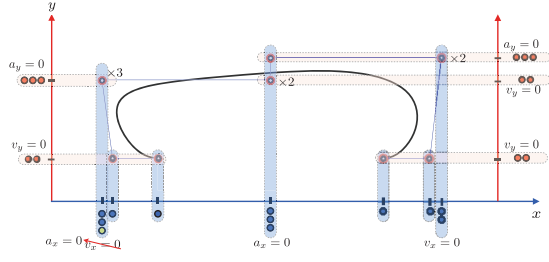


Fig. 7. Separation of twelve control points of Bézier curve for swing-phase trajectory into vertical direction and horizontal direction.

(ground clearance). It is parameterized by a corresponding swing-phase signal, $S_i^{\text{sw}} \in [0, 1]$ as:

$$p_i^{\text{sw}}(t) = p_i^{\text{sw}}(S_i^{\text{sw}}(t)) = \sum_{k=0}^n c_k B_k^n(S_i^{\text{sw}}(t)) \quad (20)$$

$$v_i(t)^{\text{sw}} = \frac{dp_i}{dS_i^{\text{sw}}} \frac{dS_i^{\text{sw}}}{dt} = \frac{1}{\hat{T}_{\text{sw}}} \frac{dp_i}{dS_i^{\text{sw}}}, \quad (21)$$

where $B_k^n(S_i^{\text{sw}}(t))$ is the Bernstein polynomial of degree n , $(n + 1)$ is the number of control points (12 in this paper), $c_k \in \mathbb{R}^2$ is a k -th control point where $k \in \{0, \dots, 11\}$.

Horizontal (x) and vertical (y) positions of control points are designed independently with respect to the hip/shoulder joint, considering the properties of Bézier curves. The details are described in Appendix D. In the vertical direction:

1. Double overlapped control points, $c_{0,y}$ and $c_{1,y}$, are used for zero vertical velocity with respect to a shoulder/hip joint at legs' LO.
2. For transition from “follow-through” to “protraction,” the force direction is changed by triple overlapped control points.
3. During “protraction,” double overlapped control points change the direction of the trajectory.
4. For the smooth force transition to “swing-leg retraction” in the y -direction, the acceleration direction is changed by triple overlapped control points.
5. Double-overlapped control points, $c_{10,y}$ and $c_{11,y}$, are used for zero vertical velocity with respect to a shoulder/hip joint at legs' TD.

The total 12 required control points are shown in Figure 7 as red circles.

In the horizontal direction, the leg initially has “follow-through,” changes the direction, has “protraction,” changes direction again and has “swing-leg retraction” sequentially. Therefore:

1. The horizontal velocity at LO is proportional to the difference between $c_{0,x}$ and $c_{1,x}$.
2. To change the direction after “follow-through,” double-overlapped control points are positioned.

Table 2. 12 control points for Bézier curve for designing swing phase trajectory.

	x (mm)	y (mm)
c_0	-200.0	500.0
c_1	-280.5	500.0
c_2	-300.0	361.1
c_3	-300.0	361.1
c_4	-300.0	361.1
c_5	0.0	361.1
c_6	0.0	361.1
c_7	0.0	321.4
c_8	303.2	321.4
c_9	303.2	321.4
c_{10}	282.6	500.0
c_{11}	200.0	500.0

3. During protraction, the acceleration direction is changed. Thus, triple-overlapped control points are positioned.
4. Changing direction to have “swing-leg retraction” requires double-overlapped control points.
5. The velocity of “swing-leg retraction” is proportional to the difference in the x -direction between $c_{10,x}$ and $c_{11,x}$.

Figure 7 shows 11 required control points as blue circles. In this paper, 12 control points are used for the horizontal direction as well as the vertical direction for single instruction multiple data streams (SIMD), a fast and efficient computation algorithm, by coping with Bézier control points as a 12×2 array.

The 12 control points for the designed foot-end trajectory are listed in Table 2. Satisfying the requirements described above, the swing-phase foot-end trajectory of the front right leg, for example, is designed to create ground clearance of 150 mm in the middle of “protraction,” a swing-leg retraction speed of 3.86 m/s with prescribed $\hat{T}_{\text{sw}} = 0.25$ s, $L_{\text{span}} = 200$ mm, and $P_0 = (0 \text{ mm}, 500 \text{ mm})$ as in Figure 6. If the body reference frame coincides with the inertial reference frame (see Figure 2), the legs’ angle of attack at the TD with the designed foot-end trajectory is set to be 68 deg with $L_{\text{span}} = 200$ mm, referring to the biological data of a trotting dog (Gross et al., 2009). To adjust the stroke length, the stroke length multiplier λ_{stroke} is introduced to an operator such that the robot has the modified half of the stroke length, $L_{\text{span}} = \lambda_{\text{stroke}} \times 200$ mm, which leads to a change in the legs’ angle of attack. The first column in Table 2 is scaled by λ_{stroke} to adjust the stroke length.

3.2.2. Design of the trajectory in the stance phase. The stance-phase control of each leg directly affects the performance of quadruped locomotion via interaction with the ground. The robot body dynamics results from net horizontal impulses and net vertical impulses exerted by the four legs. To achieve periodic motion of the center of mass of

the body in the vertical direction during running, the following vertical momentum conservation equation must be satisfied:

$$mgT_{\text{stride}} = \sum_{\text{contact}} \int_0^{T_{\text{st}}} F_{\text{ext}}^n(t) dt \quad (22)$$

where m is the robot mass, T_{stride} and T_{st} are the actual stride period and actual stance-phase period, respectively, and F_{ext} are external forces, i.e. GRFs. While maintaining the sum of vertical impulses, the redistribution of vertical impulses to each leg is necessary because the combination of net horizontal impulse and net vertical impulses induce pitch moment to the robot (Lee et al., 1999).

The direct force control for stabilization of the robot's body dynamics is challenging because nonlinear coupling between variables such as T_{st} , T_{stride} , and F_{ext} in equation (22) require a well-defined model with minimal model uncertainties. Moreover, to compute and generate desired force vector profiles at each foot-end correctly, either exact measurement of the robot orientation or reliable state estimation, which requires concurrent regulation for accumulated error, is necessary.

Due to these underlying difficulties, a stance-phase control in this paper is designed in local coordinates, only with feasible sensory feedback such as kinematic data measured by joint encoders. As we mentioned above, we create virtual compliance in four legs to employ a possible advantage of the self-stabilizing characteristic. This virtual compliance provides an effective way to solve the complex problem of contact force control, the *equilibrium point hypothesis* (Bizzi et al., 1992). The equilibrium point hypothesis proposes that animals might exert proper force on the environment by controlling the equilibrium point of their limbs' virtual compliant system to have a penetration depth into a contact surface. Then, the instantaneous difference between the actual position on the ground and the equilibrium position in the designed trajectory generates the requisite GRFs without solving complex inverse dynamics problems. Therefore, the stance-phase trajectory has to be designed from a different standpoint than the swing-phase. Rather, the stance-phase trajectory should be the trajectory of equilibrium points for the virtual leg compliance.

The trajectory tracking error in the stance phase is mainly induced by the GRF, due to the interaction with the ground. The impedance control realized by the leg controller generates reactive forces at the foot-end according to the displacement/velocity errors at the foot-end. The integration of the generated forces by the contact legs during the stance period is the impulse as expressed in the right-hand side of equation (22).

We believe that the leg force of the fast running robot exerted on the ground can be modulated through adjusting the penetration depth of the virtual reference trajectory into the ground, as shown in Figure 8, where y_r and y_e are the vertical components of a desired trajectory, and the ground level. Especially at high speed, leg dynamics

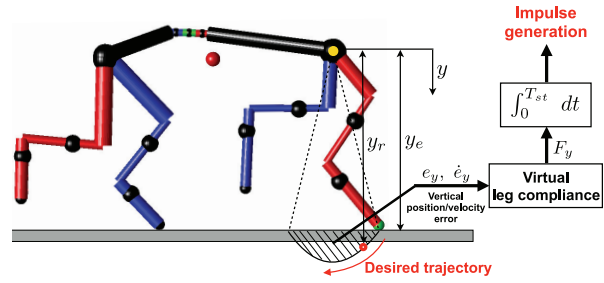


Fig. 8. Stance-phase trajectory design with equilibrium-point hypothesis; along with the vertical axis, the tracking error between the actual foot-end position and the designed foot-end trajectory is converted into the vertical force incorporated with the leg compliance. The time-integration of the force during the stance period is the vertical impulse.

are significantly faster than body dynamics, and the shoulder/hip height y_e is almost stationary while the robot's leg is moving. When this assumption is effective, as shown by vertical leg length experimental data in Figure 32 in Section 6, the shape of the trajectory error in the vertical direction follows that of the desired trajectory. Therefore, the vertical force exerted to the ground is determined by the virtual impedance as well as the stance-phase trajectory. If an implementable gain set for the impedance control is predefined, it is possible to adjust the vertical impulse exerted on the ground during the stance period through the design of the trajectory (Jung et al., 2004).

The stance-phase trajectory is proposed to simply as a sinusoidal wave with two parameters, as depicted in Figure 6: (a) half of the stroke length, L_{span} , and (b) amplitude variable, δ . Based on the phase signals, S_i^{st} , the reference foot-end trajectory of each leg is generated during \hat{T}_{st} . Stance-phase trajectories for each leg are parameterized by the corresponding phase signal, $S_i^{\text{st}} \in [0, 1]$ as

$$p_{i,x}^{\text{st}}(t) = L_{\text{span}}(1 - 2S_i^{\text{st}}(t)) + P_{0,x} \quad (23)$$

$$p_{i,y}^{\text{st}}(t) = \delta \cos\left(\frac{\pi}{2L_{\text{span}}} p_{i,x}(t)\right) + P_{0,y} \quad (24)$$

$$v_{i,x}^{\text{st}}(t) = \frac{dp_{i,x}}{ds_i^{\text{st}}} \frac{ds_i^{\text{st}}}{dt} = -\frac{2L_{\text{span}}}{\hat{T}_{\text{st}}} \quad (25)$$

$$v_{i,y}^{\text{st}}(t) = \frac{dp_{i,y}}{dp_{i,x}} \frac{dp_{i,x}}{dt} = \frac{\delta\pi}{\hat{T}_{\text{st}}} \sin\left(\frac{\pi}{2L_{\text{span}}} p_{i,x}(t)\right) \quad (26)$$

The vertical stance-trajectory is designed by using a sinusoidal wave with its amplitude δ which determines y_r when y_e is almost stationary in Figure 8. We intend to simply modulate GRFs for the robot's running, through tuning the amplitude, δ of a sinusoidal wave for the stance control, especially for a trot gait which shows, in general, small pitch variation. The higher δ is, the deeper the penetration of the desired stance trajectory into the ground, and, therefore, the net vertical impulse during the stance phase can be increased.

The stance-phase trajectory in the horizontal direction is designed under the assumptions that the foot does not slip and that the velocity of the shoulder/hip relative to the foot-end is constant as the desired velocity during \hat{T}_{st} . L_{span} approximates a half of the distance traveled by a hip/shoulder during each stance phase. Therefore, the robot retracts the foot-end in the stance phase by L_{span} with the constant speed, v_d in equation (11). To guarantee continuity at transitions between stance and swing phases, both control parameters, L_{span} and \vec{P}_0 , are set to be identical to design of the swing-phase trajectory.

A series of harmonic functions can create various shape of trajectories with a few parameters which can generate different impulses. In this paper, only a sinusoidal stance-phase trajectory is generated, with the amplitude, δ , as a control variable for trot gait. We expect a higher-order series can be used for asymmetric gait-pattern.

3.2.3. Scaling and translation of the designed trajectory. Once the reference trajectory is defined, additional four DoFs are permissible to the operator for adjusting the predesigned reference trajectory in order to adapt to the environment. The four parameters are translations of the reference point \vec{P}_0 in the horizontal and vertical directions, scaling of the entire trajectory in horizontal direction, and penetration depth δ . The potential usage of $P_{0,x}$ is inspired by Hodgins and Raibert (1991). For trot, the value is set to zero, but further investigation is required for gallop, where more aggressive acceleration and deceleration per step is likely to be realized.

3.3. Low-level individual leg controller

The impedance control is introduced to each leg controller on the proprioceptive force control actuators for two main reasons: to provide virtual compliance during the stance phase—the enabling condition for the self-stability—and to accomplish motion tracking control in the swing phase without addressing computationally expensive inverse kinematics or inverse dynamics. Since the impedance controller provides stable motion control and effective interaction control, we can avoid the complex problem of switching between stance and swing control, which involves exact event detection.

A virtual compliant leg system could be realized as the visco-elastic model of a muscle, without installing any mechanical spring and damper on the leg. For that, the agility of the mechanical and electrical leg system enables the low-level leg controller to impose a programmable virtual leg impedance despite the rapidly time-varying equilibrium point. The mechanical bandwidth of the robot's leg in the radial direction is measured to be 57 Hz with efforts to minimize the leg's mechanical impedance and to use low gear reduction ratio by increasing the motor's torque density. The legged robot inevitably has ground impact, which generates a wide frequency range of disturbance. In order

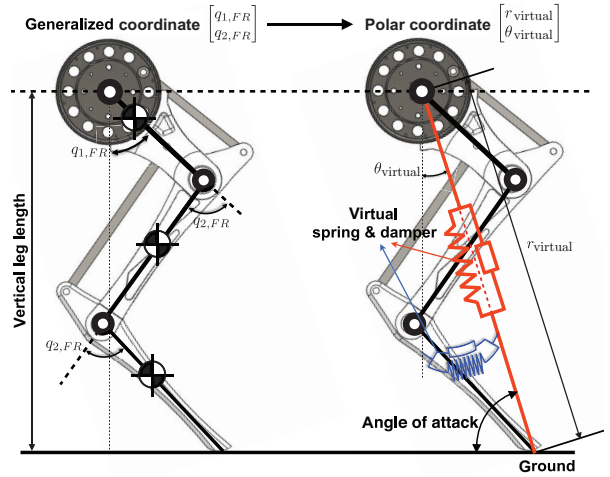


Fig. 9. Front leg with the impedance control; virtual leg compliance realization with programmable stiffness and damping for radial/angular directions.

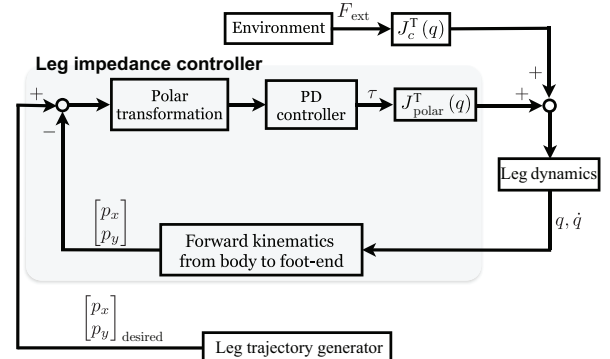


Fig. 10. Block diagram for leg controller; implementation of the impedance control to create virtual leg compliance.

to stabilize such a leg system and create virtual compliance, the fast sample rate for the overall closed loop is required; therefore an FPGA/RT-based control architecture is constructed to achieve a 4 kHz control sample rate.

Virtual leg impedance is created in the polar coordinate as in Figure 9. The *virtual leg* is defined as the straight line from the shoulder/hip joint to the foot-end of each leg. Imposing this virtual spring and damper allows for adopting results from biological examinations, simplified dynamic model studies and previous robotic experiments with mechanical springs installed on legs, such as the proper value for leg stiffness and angle of attack.

Figure 10 shows the block diagram for an individual leg impedance controller implemented on the real robot. Based on the measurement of joint positions by the rotary encoders, a foot-end position/velocity can be computed by using the leg forward kinematics and Jacobian, with respect to a shoulder/hip, respectively.

The Cartesian position and velocity errors in trajectories are transformed to the polar coordinate and multiplied with

the predefined impedance to calculate torque commands for each motor as:

$$u = J_{\text{polar}}(q)^T \begin{bmatrix} K_{p,r}e_r + K_{d,r}\dot{e}_r \\ K_{p,\theta}e_\theta + K_{d,\theta}\dot{e}_\theta \end{bmatrix} \quad (27)$$

where e_r , \dot{e}_r , e_θ , and \dot{e}_θ are radial position error, radial velocity error, angular position error and angular velocity error, and J_{polar} is the Jacobian from hip to foot-end.

4. Simulation results

We evaluated the performance of the developed controller in our simulator before implementing it on the real machine. With the proposed control framework, steady-state periodic locomotions of the robot are found for various speeds, and the local stability of each limit cycle is investigated. Lastly, simulation of multiple strides in the presence of initial large perturbations shows sufficient basins of attraction of the limit cycles, which implies the self stability.

The dynamic simulation with the robot model, periodic steady-state motion search, and local stability analysis are conducted in MATLAB R2013a (Mathworks Inc.). The constrained EoMs with inelastic impact and Coulomb friction models, derived in Section 2, are numerically integrated using the `ode45` solver with `RelTol` 1e-6 and `AbsTol` 1e-6.

4.1. Control parameters for the simulation

A control strategy with the developed controller introduced in the previous section was verified in the simulation and applied to the experiment. The strategy is quite simple; we first search a suitable set of parameters explained in Table 1, which provides stable locomotion at a value of speed, 4.5 m/s, the minimum target speed, and then increase/decrease the robot's speed by changing the parameter v_d .

We mainly adjust two control parameters, penetration depths for stance phase trajectory $\delta = (\delta_F, \delta_B)$, to stabilize the body pitch while observing the locomotive behavior of the robot model. The other parameters such as leg compliance and swing trajectories are predetermined as follows. Referring to the dimensionless analysis of “relative leg stiffness” of running animals (denoted as $k_{\text{rel,leg}}$ in Blickhan and Full (1993)), the virtual radial stiffness of each leg of the robot was set to be 5 kN/m. The gain values for radial damping ($K_{d,r} = 100$ Ns/m), angular stiffness ($K_{p,\theta} = 100$ Nm/rad), and angular damping ($K_{d,\theta} = 4$ Nms/rad) were obtained from preliminary single leg experiments (Seok et al., 2012). The swing trajectories for four legs were set to be identical by sharing the same set of control points for the Bézier curve. The half of the stroke length, L_{span} , is determined as 170 mm for all legs retaining increasing margin of the stroke length, by setting the parameters $\lambda_{\text{stroke},F}$ and $\lambda_{\text{stroke},B}$ to be 0.85, which corresponds to legs' angle of attack of 71 deg.

Table 3. A set of control parameters designed for the simulation.

Gait pattern modulator	
Terminology	Value
\hat{T}_{st}	Varies according to equation (11)
\hat{T}_{sw}	0.25 s
$\Delta \vec{S}_{\text{trot}}$	[0.5, 0.5, 0] ^T
Leg trajectory generator	
Terminology	Value
\mathcal{B}_F	Bézier control points in Table 2
$L_{\text{span},F}$	170 mm ($\lambda_{\text{stroke},F} = 0.85$)
δ_F	36 mm
$P_{0,F}$	(0 mm, -500 mm)
\mathcal{B}_B	Bézier control points in Table 2
$L_{\text{span},B}$	170 mm ($\lambda_{\text{stroke},B} = 0.85$)
δ_B	10 mm
$P_{0,B}$	(0 mm, -500 mm)
Leg impedance controller	
Terminology	Value
$K_{p,r}$	5000 N/m
$K_{d,r}$	100 Ns/m
$K_{p,\theta}$	100 Nm/rad
$K_{d,\theta}$	4 Nms/rad

In the simulation, the periodic steady state locomotion at a target speed, 4.5 m/s, is initially found with the control parameters listed in Table 3. The parameters δ_F , δ_B are carefully adjusted so that two steps of trot gaits show symmetric height variation (see Figure 13, below). Snapshots of trotting simulation using these control parameters are shown in Figure 11.

To increase/decrease the forward speed of the robot model with the trot gait, the stride frequency is modulated in accordance with $v_d = \frac{2L_{\text{span}}}{\hat{T}_{\text{st}}}$ as described in Section 3. The compliance and trajectories of each leg were fixed for a range of speeds. Farley et al. (1993) observed that leg stiffness(k_{leg}) is independent on the locomotion speed. They also noted that animals such as dogs and horses increase their stride frequency linearly with speed in the trot gait. In the following analysis, the desired speed v_d is varied as mentioned above, having the other control parameters fixed.

4.2. Steady periodic running

Periodic steady-state locomotion of the robot model with the designed controller at different speeds are simulated. Instead of following trajectories of every state of the robot, we seek a function that maps states at the beginning of the k th stride to states at the $(k+1)$ th stride, i.e. stride-to-stride return map, also known as Poincaré map. This way of analyzing steady-state behavior and orbital stability is

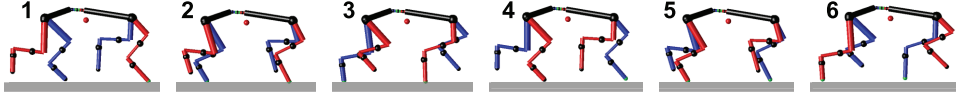


Fig. 11. Snapshots of trot-running in the simulation. Speed of the robot model's periodic steady-state is around 4 m/s.

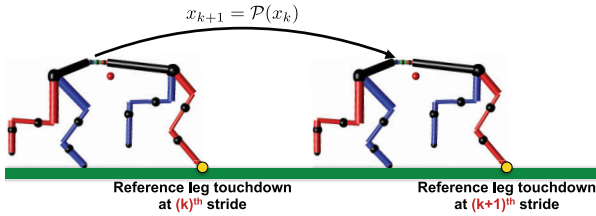


Fig. 12. Stride-to-stride return map to analyze steady-state motion and local orbital stability of the limit cycle. The instants at which the reference leg touches down to the ground define the Poincaré section.

conventional in legged robotics (Remy, 2011). The analytic expression of this mapping function is challenging for large dimensional systems, but often computed numerically by means of observing the discrete changes of states while integrating EoMs.

It is typical to choose the Poincaré section as the ground contact of a specific leg in legged machines (McGeer, 1990), and we define ours as the instants at which the reference leg touches down the ground, as it triggers the gait-pattern modulator in the controller (see Figure 12). For our 22-dimensional system, we only map 21 states: all states but horizontal displacement, since horizontal translation is not periodic and monotonically increasing. The reduced-dimension robot states for two successive TDs of the reference leg are related as

$$x_{k+1} = \mathcal{P}(x_k) \quad (28)$$

and finding limit cycle of the steady-state periodic locomotion is equivalent to finding the fixed point of \mathcal{P} .

$$x^* = \mathcal{P}(x^*) \quad (29)$$

The limit cycles of the robot, at high speeds we are interested in (3.5, 4.5, 5.5 m/s), are plotted together with the limit cycle at 2.5 m/s in Figure 13. We visualize the limit cycles in the 21-dimensional space by projecting them onto the 2-dimensional space of interest. Here, the pitch and height of the robot model (q_{pitch} , y in Figure 2) are chosen since they are most informative to describe body dynamics. To find each limit cycle, we use MATLAB `fmincon` routine of the optimization toolbox. In order to choose initial seeds for this *single shooting* optimization, we run simulation with a reasonable set of initial conditions, and evaluate the states at Poincaré section after 10 s of running.

A characteristic of the proposed gait-pattern modulator using stride-to-stride gait-pattern modulation triggered by

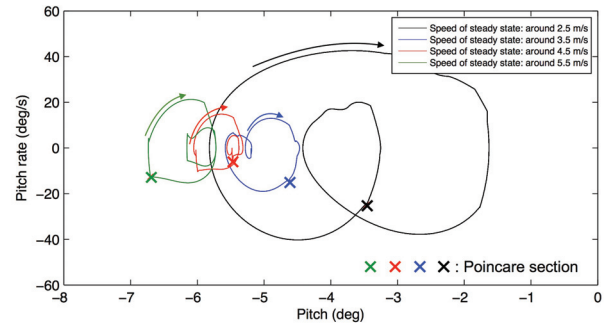


Fig. 13. Limit cycles of the robot model projected onto the robot's pitch and height phase portraits at different speeds: 2.5 m/s, 3.5 m/s, 4.5 m/s, 5.5 m/s. Poincaré sections are indicated on each limit cycle as cross marks.

the reference leg's TD, is observed in limit cycles at high speeds (Figure 13). Two steps in one periodic stride of trot gait follow different orbits in limit cycles; while we found the symmetry of two orbits at 4.5 m/s, the leading step after the TD of the reference leg (the Poincaré section) and the trailing step follow different orbits at different speeds. The robot's pitch and height variations at high speeds are small compared to the pitch and height variation at a low speed, 2.5 m/s. As the robot's speed increases, the stance period of each leg shortens. In order to satisfy the conservation of vertical momentum in equation (22), peak ground reaction forces at the foot-end is required to increase. Since $\vec{\delta} = (\delta_F, \delta_B)$ are fixed, the average body height tends to decrease, compensating these required forces. The hind legs are coupled with the spine as described in Section 2. The vertical effective impedance of the front leg is comparatively smaller than one of the hind legs. Therefore, the projected limit cycles onto the pitch phase portrait tends to move left in Figure 13 as speed increases, which implies that the robot is slightly tilted to a nose-down direction.

Table 4. Maximum magnitudes of Floquet multipliers at three different trotting speeds.

Forward speed (m/s)	Max. magnitude of Floquet multipliers
3.5	0.6898
4.5	0.6332
5.5	0.7334

4.3. Local stability of steady periodic motion

We first determine that the limit cycles we found are locally stable. The local orbital stability of a limit cycle is equivalent to the local stability of the fixed point of the Poincaré map. From the Taylor expansion, the tangent linearization of the Poincaré map about the fixed point gives:

$$x^{k+1} = \mathcal{P}(x^k) = \mathcal{P}(x^* + \Delta x^k) \approx \mathcal{P}(x^*) + (\nabla \mathcal{P}) \Delta x^k \quad (30)$$

where $\Delta x^k = x^k - x^*$ is the k th perturbation and $(\nabla \mathcal{P})$ is the gradient of the map with respect to the states computed at the fixed point. By definition $\mathcal{P}(x^*) = x^*$, and we can rewrite equation (30) as

$$\Delta x^{k+1} \approx (\nabla \mathcal{P}) \Delta x^k \quad (31)$$

The equation (31) is the linear approximation of stride-to-stride map of small perturbation about the fixed point. The $\nabla \mathcal{P}$ is known as the *monodromy matrix* of the Poincaré map and the eigenvalues of this matrix are called *Floquet multipliers*. Mathematically, if the magnitude of all Floquet multipliers are strictly less than one, the perturbation vanishes over time. The limit cycle with this property is thus stable and any phase trajectory near the limit cycle is attracted to it (Remy, 2011).

The monodromy matrices and Floquet multipliers can be numerically computed by perturbing each state and observing the return map (Goswami et al., 1997). The eigenvalues we found are shown in Figure 14. The maximum magnitude of Floquet multipliers for different values of speed are listed in Table 4. Since all eigenvalues are within the unit circle, we can conclude that the locomotion with the trot gait at each speed has a stable limit cycle. Note also that most of the eigenvalues are close to 0 since the individual leg controllers regulate perturbation in leg joint states during swing phase.

4.4. Stable trotting of the robot model with large initial perturbations

The Floquet multipliers in the previous section only concludes local stability under small perturbations. To evaluate the stability of the system under large initial perturbations, we let the simulation run with initial conditions far from steady states in the periodic locomotion and examine the data for a multiple stride time (11 s).

Figure 15 shows the self-stabilizing behavior even in the presence of large initial state perturbations such as speed,

body height, and pitch. The state of robot model successfully converges to the periodic steady-state locomotion at different desired speeds with the trot gait with the developed controller. Note that the initial perturbations are large enough to have overlapped states. Even under those large perturbations, the robot model's state converges to its periodic steady state around a commanded speed. Therefore, we concluded that the controller is able to be extended to a real machine for stable and robust trot-running. Stability at different commanded speed also implies that the acceleration strategy we introduced is applicable; changing a single parameter v_d in the controller to accelerate/decelerate the robot.

4.5. Approximation of GRFs at each foot-end: Simulation

To increase torque-transparency from the actuator to the foot-end of each leg, the leg manipulator system of the MIT Cheetah has minimized inertias with high torque-density electromagnetic motors and low gear reduction ratio (Seok et al., 2012). The minimized mechanical impedance allows estimation of the GRFs by using actuating torques, τ , as

$$F_{\text{ext}} \approx \mathcal{R}(-J_{\text{Cart}}^T(q))^{-1} \tau \quad (32)$$

where F_{ext} is the GRF, \mathcal{R} is the rotation matrix to compensate the orientation of the front/back body reference frame with respect to the inertial frame, J_{Cart} is the local Jacobian of the shoulder/hip joint to the foot-end of each leg in the Cartesian coordinate, and τ are the generated torques at the leg's joints according to the virtual leg compliance, respectively.

During steady periodic trot-running at 4.5 m/s, the GRF profiles are solved in the simulator using equation (4), and the foot-end force profiles are estimated by equation (32) for one diagonal pair of legs of the robot model, as shown in Figure 16. Solid lines and dotted lines are horizontal and vertical force components at each foot-end. Note that the solved GRFs are similar to the estimated foot-end forces in the stance periods. This result implies that GRFs can be effectively estimated from local data, leg kinematics, and torques. This approximation is also verified by a single leg drop test shown in Figure 31, below. To estimate GRFs on the real machine in the absence of force sensor, we employ this method in Section 5.

4.6. Smooth change of leg coordination for trot-to-gallop transition

Figure 17 shows the snapshots of the gait transition simulation by linearly varying the gait-pattern parameters, $\Delta \vec{S}$ over one stride time period. We applied the identical trajectory used for the trot-running, changing only the gait-pattern. If a control parameter set for the stable gallop gait can be found, the role of the gait transition is to make the states of the robot enter into a basin of attraction which the

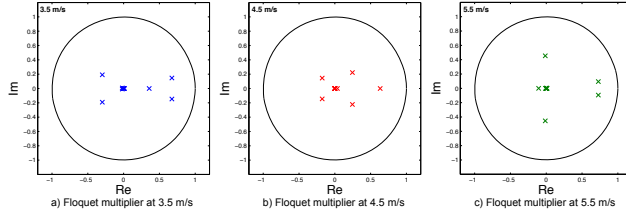


Fig. 14. Eigenvalues of the monodromy matrices at different value of speeds: 3.5 m/s, 4.5 m/s, 5.5 m/s. No eigenvalue has magnitude greater than 1, which proves local stability of each limit cycle of the robot with the proposed controller.

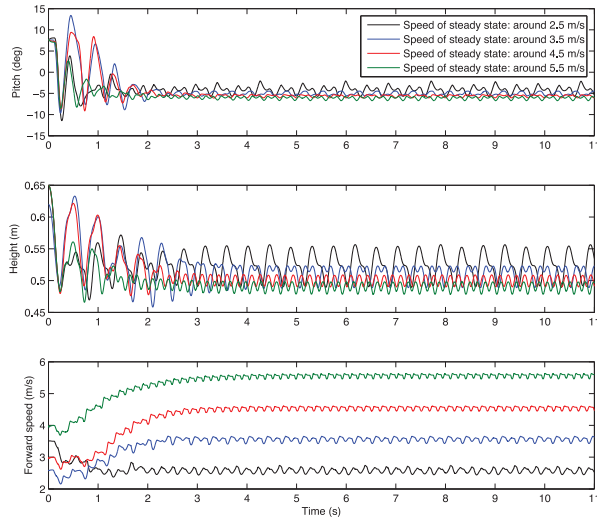


Fig. 15. Trot-running simulation performance in the presence of large initial perturbations at various speeds of steady state around 2.5 m/s, 3.5 m/s, 4.5 m/s, 5.5 m/s. Pitch (*top*), height (*middle*), and forward speed (*bottom*) are plotted over time. Perturbations are damped out as the robot approaches periodic steady-state locomotion.

galloping dynamics constructs. A loss of stability which might be induced during the gait transition have to be manageable within the stability margin of the gallop gait. Its completion is left for a following paper that addresses the galloping implementation of the MIT Cheetah, using exactly the proposed gait transition method.

5. Experiments on the MIT Cheetah

The MIT Cheetah running experiment addressed in this section demonstrated the performance of the proposed control framework on the real robot. During the experiments, the sagittally constrained MIT Cheetah was able to achieve a fast and stable trot, reaching up to about 6 m/s. The trot-to-gallop gait transition was also trialed. See Multimedia Extension 1 in Appendix Appendix A. The controller, however, was not able to stabilize the gallop gait, after the gait transition, by linearly varying the gait parameters in this experiment.

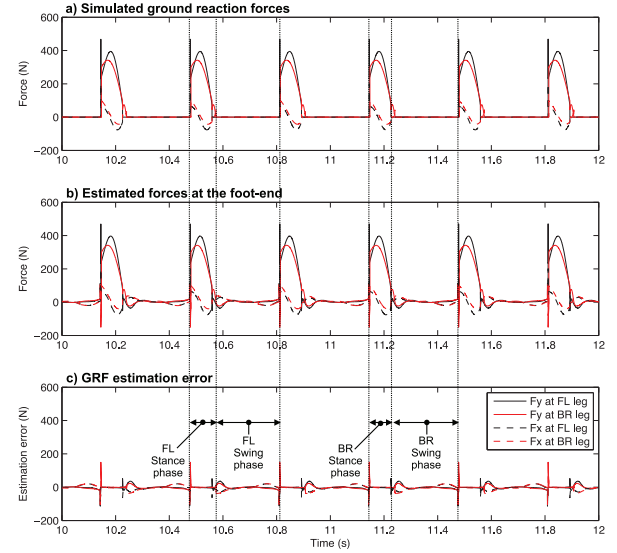


Fig. 16. (a) Simulated GRFs; (b) estimated foot-end forces; (c) GRF estimation error: force differences between the GRFs and the estimated foot-end forces when the robot model is trotting with a steady periodic motion at 4.5 m/s.

5.1. Experimental setup

The MIT Cheetah was sagittally constrained on a modified commercial treadmill (SOLE TT8) as shown in Figure 18. The treadmill motor (3.5 hp TURDAN DC.PM 90V–25A) is manually controlled by a NI sbRIO-9642 with a motor driver (Apex Microtechnology MSA260KC) to synchronize its speed with the robot running speed. The maximum speed of the treadmill is measured at 6 m/s. A minimal friction sliding guide is connected to the CoM of the robot through a revolute joint in order for the roll and yaw motion of the robot. The effective mass of the guide on the robot, 3 kg, is equivalent to the mass of the four 22.2 V serially connected LiPo batteries (465 Whrs) which were housed in the explosion-proof box outside of the robot for safety.

The only feasible sensory feedbacks on the controller were positional data for each leg joint given from the 13-bit rotary magnetic encoders installed at developed dual-coaxial BLDC motor units of each leg. Other state feedbacks of the robot were not available in the experiment. For the TD detection of the reference leg, the proposed proprioceptive feedback is set with the value of the

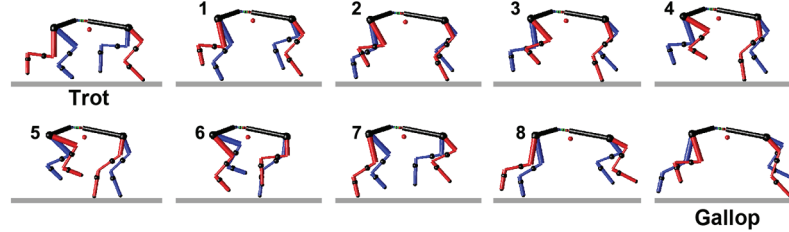


Fig. 17. Snapshots of gait transition from trot to gallop by linearly varying gait-pattern parameters $\Delta\vec{S}$ over one stride time period.

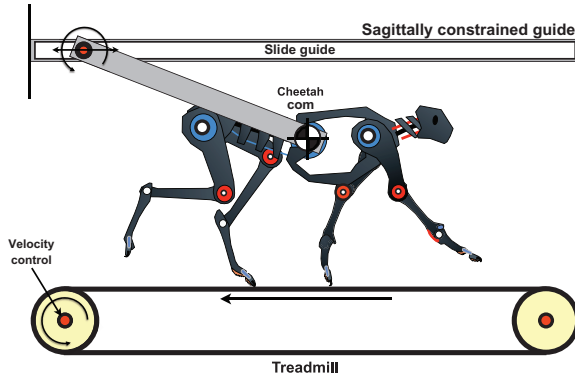


Fig. 18. Experimental setup: the sagittally constrained MIT Cheetah runs on the speed-controlled treadmill.

threshold force, 2N, which was obtained in the preliminary experiment. Four Dynamixel EX-106+ smart motors were used to control ab/adduction of each leg. Also, a customized motor driver (MCU: Microchip dsPIC30F6010) handled the current control of each motor at 20 kHz.

The hierarchical controller was implemented with 4 kHz overall closed-loop sample rate on the FPGA/RT based compactRIO (cRIO-9082) with the LabVIEW software. A wireless network (802.11 protocol) with the robot was established and the controllable parameters were able to be wirelessly adjusted by the operator through the LabVIEW front panel. All the data, such as the measured joint angles and commanded currents, were saved with the sampling rate 4 kHz through the RT FIFO memory to the embedded flash memory during the experiment.

5.2. Control parameters for the experiment

The predefined gait trajectories for the experiment are shown with respect to the shoulder joint for the front legs and the hip joint for back legs in Figure 19. Shaded regions were the workspace for each leg based on its mechanical joint limits. The control parameters for front and back legs, denoted as *F* and *B* respectively, are listed in Table 5.

The control parameters were slightly adjusted based on the parameters used in the simulation during the preliminary experiment: trot-walking at low speed. With consideration of the coupling effect between the semi-active spine and back legs, the stance trajectory design of the back legs

Table 5. A set of control parameters designed for the experiment.

Gait pattern modulator	
Terminology	Value
\hat{T}_{st}	Varies according to equation (11)
\hat{T}_{sw}	0.25 s
$\Delta\vec{S}_{trot}$	$[0.5, 0.5, 0]^T$
Leg trajectory generator	
Terminology	Value
\mathfrak{B}_F	Bézier control points in Table 2
$L_{span,F}$	170 mm ($\lambda_{stroke,F} = 0.85$)
δ_F	36 mm
$P_{0,F}$	(0 mm, -500 mm)
\mathfrak{B}_B	Bézier control points in Table 2
$L_{span,B}$	170 mm ($\lambda_{stroke,B} = 0.85$)
δ_B	0 mm
$P_{0,B}$	(0 mm, -550 mm)
Leg impedance controller	
Terminology	Value
$K_{p,r}$	5,000 N/m
$K_{d,r}$	100 Ns/m
$K_{p,\theta}$	100 Nm/rad
$K_{d,\theta}$	4 Nms/rad

was conservatively designed just as flat simply by describing $\delta_B = 0$, which is discussed in Section 6. $P_{0,F}$ and $P_{0,B}$ were designed with consideration given to the stable attitude of the robot in the static posture. With this designed foot-end trajectory with $L_{span} = 170$ mm ($\lambda_{stroke} = 0.85$), the swing-leg retraction speed was set to be 3.4 m/s by the property of the Bézier curve.

5.3. Experimental results

The MIT Cheetah was able to accelerate up to 6 m/s with the trot-gait-pattern according to the operator's forward speed command. A stable running was observed over the range of recorded velocity, with the trot footfall pattern as in Figure 20 in the experiment. At low speed the robot walked with

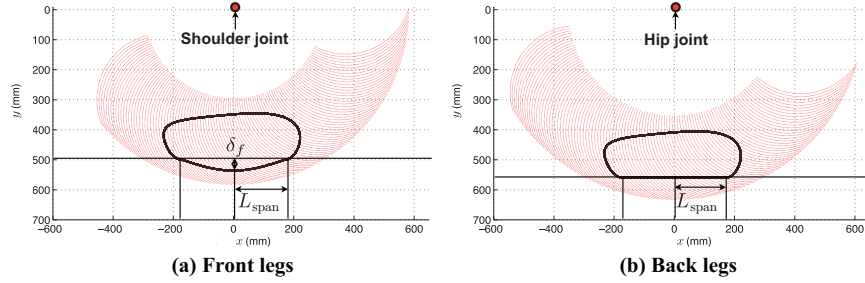


Fig. 19. The leg trajectories implemented on the experiment within the allowable workspace (red shaded region) of the MIT Cheetah.

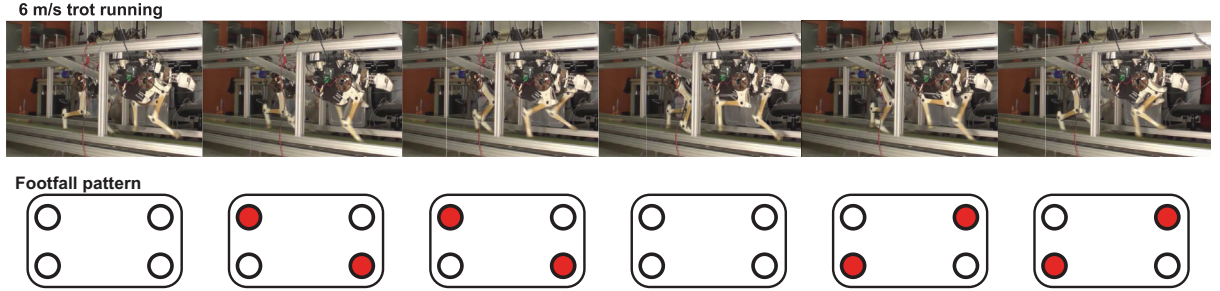


Fig. 20. Snapshot for the trot-running gait of the MIT Cheetah with each footfall diagram; the existence of the aerial phase is observed between each step of a leg pair in trotting gait.

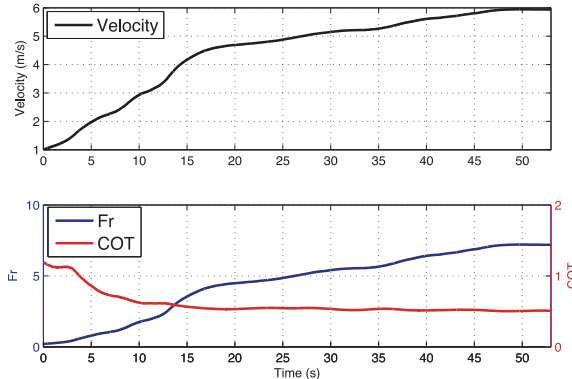


Fig. 21. Estimated forward velocity (top) of the MIT Cheetah: ± 0.15 m/s bounded difference was observed between the estimated speed and the treadmill speed measured by a rotary encoder (CUI Inc. AMT 102-V) directly attached to the DC motor's main axis. Fr (bottom, blue solid line) and COT (bottom, red solid line) of the robot are plotted together.

trot gait, but as speed increased the robot transitioned to running around 2.2 m/s, which corresponds to $Fr \approx 1$ where centrifugal force and gravitational force match.

5.3.1. Estimated locomotion speed. Figure 21 shows the estimated forward speed of the MIT Cheetah based on the measured kinematic data during the experiment. The controlled-stance phase period (\hat{T}_{st}) for each leg was determined by the desired speed. Comparing the observed speed of the treadmill with the estimated speed of the robot, the difference was smaller than 0.15 m/s. As shown in the

velocity plot, the robot initially accelerated fast up to 4.5 m/s, and then smoothly speeds up to 6 m/s during 50 s. The non-dimensional metrics, Fr and COT, are shown together in the graph below. Around the robot's maximum estimated speed of 6 m/s, the Fr was 7.34 and COT was 0.5, rivaling legged running animals.

5.3.2. Measured leg trajectories. Figure 22 shows trajectories of all four legs measured over various speeds during the experimentation. The identical angle of attack at legs' TD is desired to be 71 deg for all legs with the fixed $\lambda_{stroke} = 0.85$ that was used in the simulation. In order to increase speed, an operator decreases \hat{T}_{st} to increase the stride frequency of the trot gait. The leg trajectories are plotted when each shoulder or hip joint is (0, 0) in the body local coordinates. The data support that both the pitch and height of the frontal body fluctuate slightly during the experiment. Slight pitch variation at the beginning and the end of the swing phase can occur due to effect of the coupling mechanism between the hind legs and the spine. The top-left subplot shows the desired trajectory. Again, the shape of the desired trajectory remained the same over different target speeds. Note that the short-cut swing-to-stance transition, the short straight line connecting the end region of the swing-phase trajectory and the beginning region of the stance-phase trajectory, was observed as shown in Figure 23 due to early TD detection after 90% completion of the swing phase.

The top-right subplot expands the actual trajectories with respect to its achieved speeds. As speed goes up, the vertical width of the trajectory closed-loop decreases and shoulder/hip heights in the stance phase decrease. This results

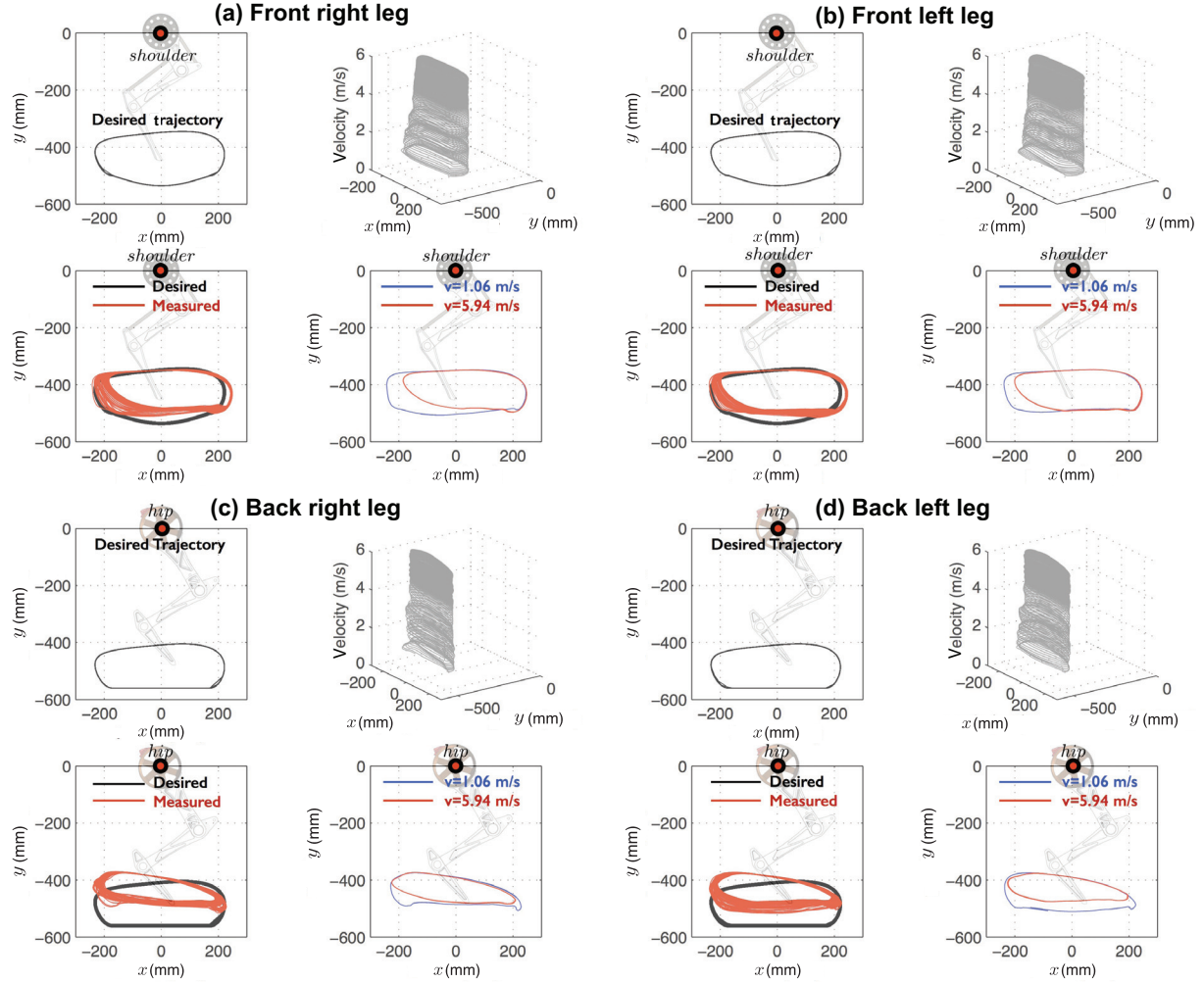


Fig. 22. Desired trajectories by the leg-trajectory generator and measured actual gait trajectories during trotting gait from 1 to 6 m/s for (a) front right leg, (b) front left leg, (c) back right leg, and (d) back left leg. In each leg graph, *top-left*: desired trajectories; *top-right*: actual trajectories with respect to speed; *bottom-left*: comparison between desired/actual trajectories; *bottom-right*: comparison between actual trajectories at low/high speeds, respectively.

in smaller duty factor that requires higher vertical forces at stance legs to provide the necessary vertical impulse for running, as explained in equation (22). The bottom-left subplot compares the desired trajectory and the measured trajectory. It shows the tracking performance of the impedance control for the swing phase; the trajectory converges within 25% of the duration of the entire swing phase. On the other hand, for the stance phase, the impedance control exerted high enough forces to make the robot run, due to the positional errors in stance-phase trajectories. Stance-phase performance will be discussed below together with the foot-end force plot in the Cartesian coordinate. The bottom-right plot compares the measured trajectory at low speed and high speed. The relatively flat portion of the trajectory indicates ground-contact. The apparent conclusion is that as the target speed increased, the distance that shoulder/hip traveled in the stance phase was shorter than the design called for.

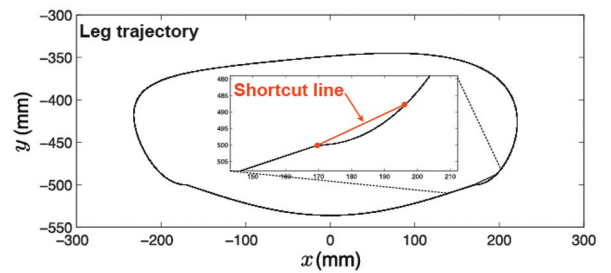


Fig. 23. The shortcut line at the swing-to-stance transition on the desired trajectory for the front left leg, the reference leg, is observed due to the early TD detection of the reference leg.

A coupling effect of back legs with the spine through the differential gear was observed in the measured back-leg gait trajectories. This effect led to a deviation of the actual trajectories away from the desired trajectory, even during the swing phase where there was no interaction with the

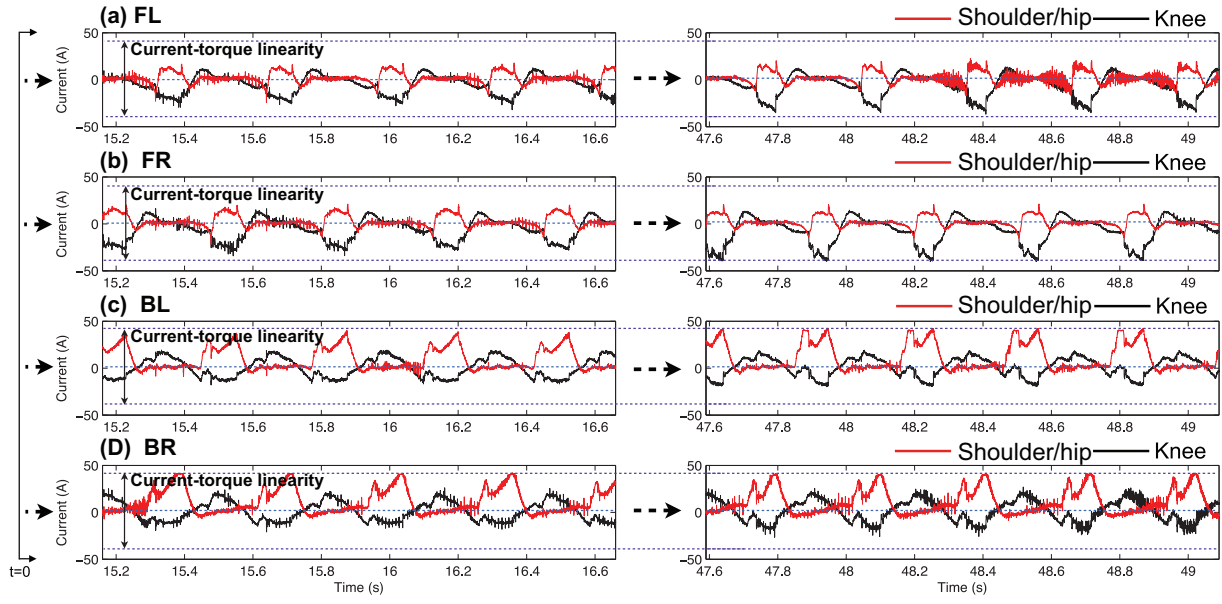


Fig. 24. Raw data of the commanded currents applied to each EM motor for shoulder/hip and knee joints at leg $i \in \{\text{FL}, \text{FR}, \text{BR}, \text{BL}\}$ with the region where linearity between current and torque is conserved with the torque constant K_t in $\sim -40\text{--}40$ A.

ground. Therefore, improving the tracking performance of the back legs, which are coupled with the spine, requires accurate modeling of the back legs-spine system.

5.3.3. Estimation of generated leg-force based on applied currents to the actuators. Investigating the interaction between the robot and the environment should require the analysis of forces generated at the foot-end of the robot. However, the experiment was performed without a force plate on/under the treadmill and without any force sensor at the foot to measure GRFs. Nevertheless, the forces exerted at the foot-end can be accurately estimated by the joint torques generated from the impedance control law, as has been demonstrated in the simulation and in Seok et al. (2012). Each joint torque can be estimated by the amount of the commanded currents at the customized motor driver for the MIT Cheetah considering actuation transmission and pantographic leg design as shown in Section 6.4.

The currents at each actuator are precisely measured for the entire experiment. Figure 24 shows commanded currents provided to the dual-coaxial electric motors at the robot's shoulder/hip, for 1.5 s at different speeds (4.1 m/s and 5.9 m/s). These two time periods are selected for fair comparison between different speeds, because the robot CoT, an indicator of efficiency, was similar. As the speed increases, the increment in the amount of the current applied to the knee motor was observed.

Note the difference between currents at low speed and at high speed, as well as for front legs and back legs. A contralateral symmetry is observable in the graphs, which is the characteristic of the symmetric gait-pattern, the trot.



Fig. 25. Snapshots of leg coordination change for the trot-to-gallop gait transition recorded at 500 fps.

Increase in peak current and decrease in duration of the high-current region are observed at a higher speed. The currents measured at the electromagnetic motors at the back leg are generally much higher than currents at the front legs, because some amount of the electric current applied to the actuators at the back leg are spent for friction and compliance introduced by the cable-driven differential gear mechanism which couples back legs and spine.

5.3.4. Change of leg coordination. The leg coordination changing method for the trot-to-gallop gait transition proposed in Section 3 was tested on the MIT Cheetah as shown in Figure 25. At the maximum speed of 6 m/s in the experiment, the robot was commanded to change its gait from trot to gallop and it was recorded by a high-speed camera. See Extension 1. Figure 26 shows the phase signals for all legs when the gait-pattern modulator linearly changes its phase lag parameters from trot to gallop in the predefined period, 2.5 s. The smooth gait transition was observed, but the robot failed to maintain the gallop gait-pattern after a few strides. However, this is a preliminary result; further

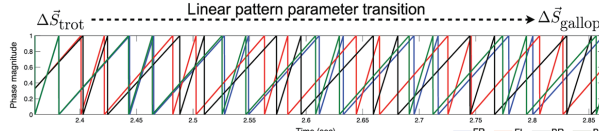


Fig. 26. Sawtooth phase signals generated by the gait-pattern modulator for the trot to gallop gait transition. The phase signal converges from one to another, linearly with time.

research explores the possibility of reaching a stable gallop after a smooth gait transition in a following paper; with this gait transition strategy, the MIT Cheetah achieved trot and gallop before/after the gait transition at 3.2 m/s as shown in Appendix G.

6. Discussion

Based on the logged data such as commanded current values, commanded/measured leg joint positions at the 4 kHz sample rate, key features of the implemented running gait on the robot are discussed; (a) estimated pitch variation, (b) measured Fr and COT in the MIT Cheetah running, (c) Walk-to-run transition and aerial phase, (d) Estimated forces exerted at each foot-end.

6.1. Estimated pitch variation

Effective indices for locomotive stability in the sense of limit-cycle can be body height and pitch variations. It is hypothesized that the stable trot gait has small repetitive fluctuations of body height and pitch. These height and pitch fluctuations can be estimated with measured foot-end trajectory data for four legs as shown in Figure 27. The flat regions of the measured foot-end trajectories are due to interaction with the ground, and therefore represent the stance phase. The height of each shoulder/hip joint is equivalent to the distance between shoulder/hip joint and foot-end positions in the stance phase at instant. Therefore, the pitch variation can be deduced from difference between front and back height data, considering the shoulder-to-hip horizontal distance, 66 cm.

During trotting, the heights of both shoulder/hip joints are observed to remain around 0.5 m. Maximum estimated height difference between a pair of legs for trot is roughly smaller than 4 cm at low speed and 2.5 cm at high speed. The estimated pitch variation decreases as locomotion speed increases. Maximum pitch variation is estimated to be 4 deg at low speed and only 2.2 deg at high speed. This small pitch variation shows the self-stabilizing behavior in the trot gait. Since virtual compliance exerts force proportional to error in displacement/velocity at each foot-end, if a large pitch motion occurs, the force exerted by the front/back legs naturally adapts to induce pitch moment to cancel out the disturbance.

For the same reason, as forward speed increases, the stance height of a shoulder/hip joint gets lower as shown

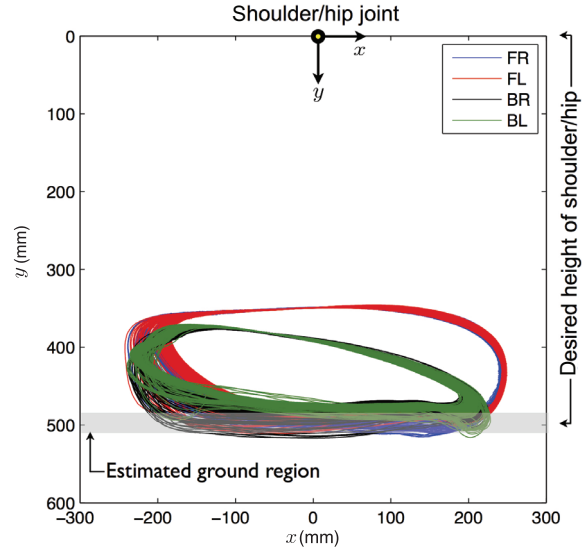


Fig. 27. Actual measured trajectories of four legs with respect to each shoulder/hip joint, where all the trajectories for the four legs are overlapped with respect to each shoulder/hip joint. The data allow us to approximate the height/pitch variation of the robot during the trot experiment.

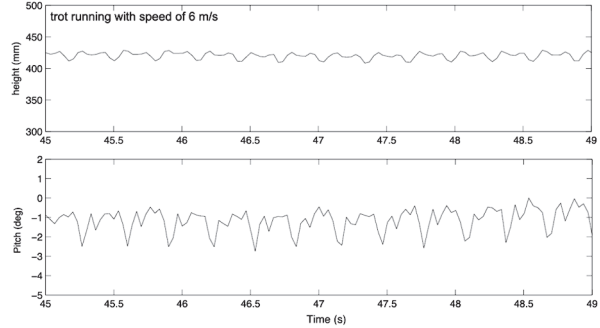


Fig. 28. CoM height and body pitch of the MIT Cheetah running on the treadmill with speed of 6 m/s, estimated by a TRACKER software with resolution of 1.4 mm/pixel.

in the trajectory vs speed plots for all legs in Figure 22. In the experiment, each desired leg-trajectory was identically applied to front/back legs over different speed ranges. At higher speed, larger vertical forces are required within shorter stance periods to satisfy momentum conservation in equation (22). Therefore, the average height of the body is observed to slightly decrease as speed increases to compensate required forces with the fixed leg compliance.

A TRACKER software⁴ was also used to estimate the CoM height and the body pitch variation at 6 m/s in the video VII of Extension 1. A similar height pattern observed in the simulation were obtained as shown in Figure 28. The maximum/minimum CoM height and body pitch were observed as 435/408 mm and $-0.07/-2.68$ deg in the time window of Figure 28, while the MIT Cheetah was running at 6 m/s, which implies that the achieved trot-running at 6

m/s has a body height variation smaller than 2.7 cm, and a body pitch variation smaller than 2.61 deg.

6.2. Measured Fr and COT of the MIT Cheetah

Nondimensional metrics such as the Fr (Kim et al., 2006; Spröwitz et al., 2013) and COT (Tucker, 1975) are often used to appropriately compare different sized legged robots and animals. Fr is size-independent locomotion speed, as defined as below

$$\text{Fr} = \frac{v^2}{gh} \quad (33)$$

where v is a characteristic (forward) speed of the locomotion, g is the gravitational acceleration, and h is a characteristic length (Alexander, 1984).⁵ For legged robots and animals, h is usually chosen as the shoulder/hip height; in the case of the MIT Cheetah, h is assumed to be 0.5 m from Figure 27.

The maximum Fr of the MIT Cheetah is 7.34. This is a remarkably high value in comparison to other quadruped robots according to the given data in Spröwitz et al. (2013); in 2013, the Cheetah-cub's Fr was 1.30, and in 2011, the HyQ's Fr was 0.6. Back in 1990, Raibert's quadruped showed an Fr of 1.53. Also, the MIT Cheetah's Fr with the trot gait is higher than the Fr observed in animals' trot gait. Biological data have shown that quadruped animals transit their gait from walk to trot at $\text{Fr} \approx 1$ and from trot to gallop around $\text{Fr} \approx 2$ or 3 (Alexander, 1984). It is also observed that dogs show trot-to-gallop gait transition around the speed corresponding to $\text{Fr} \approx 3$ (Maes et al., 2008). Interestingly, we achieved much higher Fr with the trot gait-pattern than animals. We think this is something to do with the differences in speed-torque performances between biological muscles and electric motors.

Indeed, we believe the maximum speed of the robot could be even higher because (a) the present maximum speed is limited by the maximum speed of the treadmill, and (b) a nominal value of the maximum continuous power of the actuators is approximately four times higher than the value of the power consumed by the running Cheetah at 6 m/s.⁶ For the analysis of energy efficiency, COT is used as a mass-independent energy/power consumption that measures the energy efficiency of the locomotion. COT is defined as

$$\text{COT} = \frac{P}{Wv} \quad (34)$$

where P is power used, W is weight of the robot, and v is locomotion speed (Tucker, 1975). For a detailed description of mechanical/electrical design approaches applied to the robot to achieve high energy efficiency, the reader is referred to Seok et al. (2013). In our calculation of CoT, the servo motor powers for legs' ab/adduction is not considered because the MIT Cheetah's running was implemented in the sagittal plane and the fixed ab/adduction angle policy to make the legs vertical in the frontal plane were used.

6.3. Walk-to-run transition and existence of aerial phase

The MIT Cheetah is estimated to have the walk-to-run transition at around 2.2 m/s, by taking the energetic criterion of running, which is introduced in McMahon et al. (1987). Figure 29 shows the vertical length of the virtual front right leg and the estimated speed in the time interval $\sim 2\text{--}10$ s during the experiment. The shoulder height can be estimated by the vertical length of the virtual leg in the stance phase for the case of the trot gait where the pitch variation is small; the convex shape of the vertical length in the stance phase (dotted rectangulars) is kinematically matched to the concave shape of the shoulder height and vice versa. Therefore, the typical concave/convex shoulder trajectory in walking/running is drawn before/after 2.2 m/s which corresponds to the $\text{Fr} \approx 1$ in Figure 21. Biological studies also have shown that at $\text{Fr} \approx 1$ (Alexander, 1984), the walk-to-run transition occurs in quadrupedal locomotion. After this transition, the COT was significantly improved.

The estimated duty factor D_{est} in Figure 30 shows the existence of an aerial phase, for the MIT Cheetah running. The duty factor for a foot is defined as the fraction of a stride for which the foot is in contact with the ground (McGeer, 1990). Therefore, a duty factor $D_{\text{est}} < 0.5$ implies that the animal or robot has an aerial phase for the trot gait. Because of the absence of a force plate in the experiment, the duty factor, D_{est} , is approximated based on kinematic data for each leg, as was the case for the pitch estimation. From the estimated duty factor plot, we can say at least that robot had the an aerial phase after time $t = 4$ s, where the speed estimation was 1.4 m/s.

6.4. Approximation of GRF at each foot-end: Experiment

To analyze the performance and characteristics of the trot-running result in the Cartesian coordinates, GRFs, the interaction forces between the robot and the ground, were estimated by using joint position data Figure 22 and commanded current data in Figure 24.

The motor driver was devised to apply a commanded current by the controller to the BLDC motors which have approximately a linear relation between motor torque and applied current below the motor's saturation level, 40 A. As shown in Figure 24, the peak current commanded for the front legs is under this saturation current level where the linearity assumption is effective. However, the torque/current linear relationship for the back legs can be deteriorated during a short duration because the peak currents are over 40 A instantly.

Torque outputs from BLDC motors were calculated based on measured currents and a measured torque constant, $K_t = 0.27 \text{ Nm/A}$. Then, because of high torque-transparency of the robot's leg, commanded forces exerted at each foot-end effectors of the robot can be estimated in

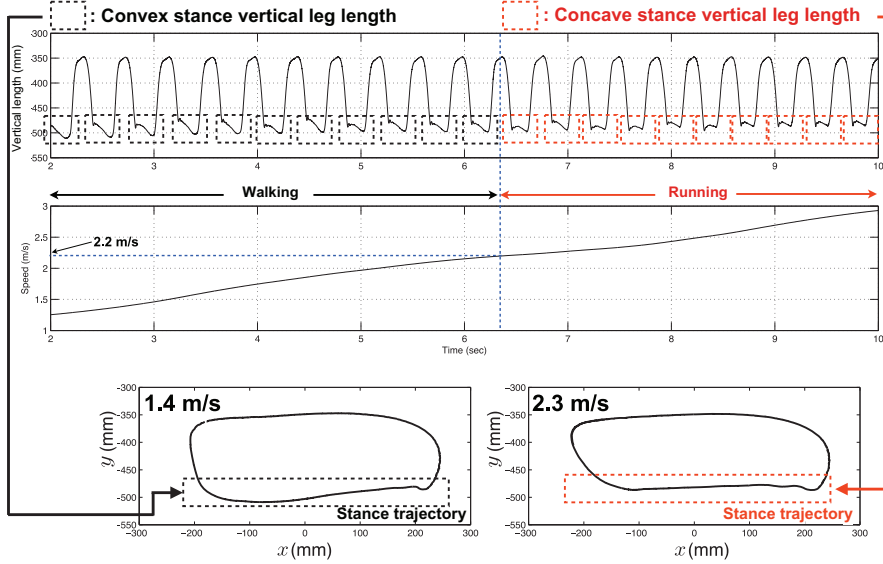


Fig. 29. Walk-to-run transition around 2.2 m/s: convex stance vertical leg length plot in the black-dotted rectangular corresponds to the robot's walking state and concave stance vertical leg length plot in the red-dotted rectangular corresponds to the robot's running state.

the front/back body reference frames as below:

$$\begin{bmatrix} F_x \\ F_y \end{bmatrix}_{\text{foot}} \approx (J_{\text{Cart}}^T)^{-1} \tau_{2 \times 1} \quad (35)$$

where J_{Cart} is the local Jacobians from shoulder/hip to foot-end of each leg of the robot. In the preliminary test, the electric bandwidth of the motor actuation system was measured to be approximately 400 Hz. Therefore, the commanded forces were filtered with the cut-off frequency of 400 Hz.

We expect that this filtered force at each foot-end calculated by equation (35) can be an effective approximation for GRFs with respect to the inertial frame, since a body pitch variation of the trot-running robot was small in the experiment.

To verify this estimation, when the one leg drops on the force sensor (ATI delta, SI- 660-60 calibration) from 5 cm height, the comparison between the vertical GRF measured by a force sensor and the commanded force in the vertical direction is shown in Figure 31. This result shows that the commanded forces are well matched to the GRFs measured by the force sensor. Therefore, the vertical force F_y and the horizontal force F_x exerted to the ground by the robot were estimated with respect to the local coordinate at each shoulder/hip joint of the leg, which is described in Figure 2. See also Extension 1 in Appendix A to watch approximated GRF patterns. Note that the effect of Cheetah leg's bending cannot be ignored at higher force ranges because the plastic material of the leg has an inherent material compliance. This effect can be shown as the difference between the estimated radial leg length given from forward kinematics, and the actual one. In a preliminary experiment, a 2 mm length difference was observed at around 350 N at the foot-end, which means that the estimated foot-end forces can

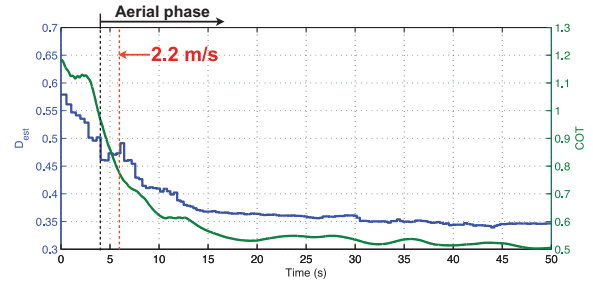


Fig. 30. Estimated duty factor D_{est} for the front right leg: measured kinematic data for the virtual leg is used to estimate the duration of the stance/swing phases. The line indicates the estimated walk-to-run transition at 2.2 m/s.

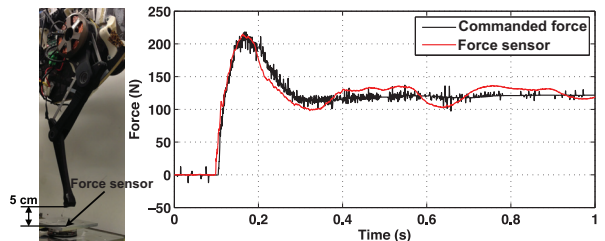


Fig. 31. Comparison of GRF and commanded force at the foot-end in the vertical direction.

deviate from the actual forces due to the the leg's bending at a force range higher than 240 N.

6.4.1. Force analysis on the front legs. Figure 32 shows the vertical motion of the front legs with corresponding desired trajectories at 6 m/s. The desired foot-end vertical trajectories penetrate into the ground in the short stance period, but the actual foot-end vertical trajectories, L_v , cannot track

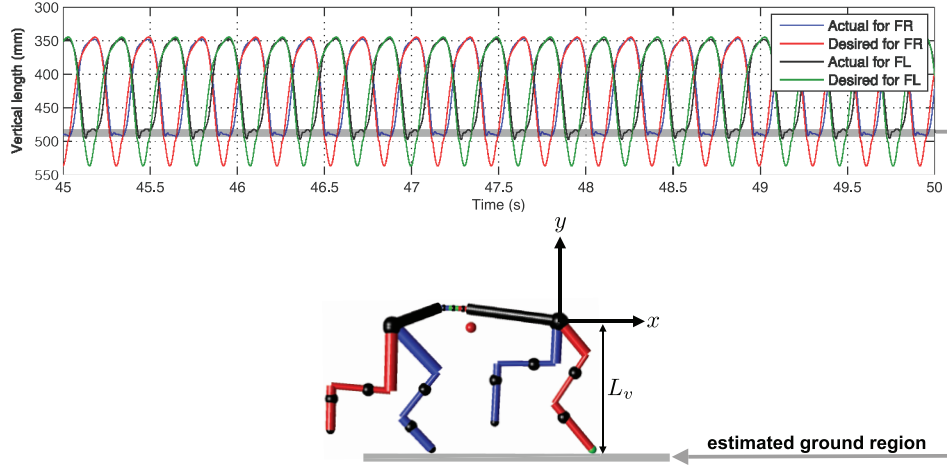


Fig. 32. Desired/actual vertical virtual leg lengths L_v .

the desired trajectory due to the ground contact. The actual trajectories remain in the estimated ground region (around 0.5 m), thus enabling the distinct separation for the stance and air phases. Therefore, the hypothesis for the stationary height of the shoulder joint during the short stance period is effective such that the height variation is smaller than 1 cm at approximately 5.9 m/s. When the leg contacts the ground, the virtual leg compliance generates vertical forces according to kinematic error intentionally induced by the proposed sinusoidal trajectory for the stance phase.

Figure 33 shows horizontal and vertical force estimations, F_x , F_y , at both front legs for each duration. High vertical force regions represent the stance phases of each leg. Characteristics of the symmetric gait-pattern, trot, are clearly observed in the graphs. Identical forces produced by the left and right sides of the legs alternate rhythmically over time, and peak value and frequency of vertical forces increase as the desired speed increases. High propulsion force, expressed as negative F_x , accompanies high vertical forces during the stance phase to compensate for impact loss.

6.4.2. Contribution of virtual damping to create virtual leg compliance. In order to quantify the effect of virtual damping in the stance control, Figure 34 shows contributions of virtual stiffness and damping separately to create virtual leg compliance while the robot were walking at a low speed, 1 m/s, and running at a high speed, 6 m/s, in the experiment. The programmable virtual leg compliance consists of the virtual stiffness (5000 N/m) and the virtual damping (100 Ns/m) and its combinational effect during the implementation is shown in Figure 37 of Appendix E. Each commanded vertical force exerted at the FR foot-end by both virtual stiffness and damping is plotted together. The virtual damping not only rejects force ripple in the trajectory-tracking control to improve transient leg dynamics in the swing phase, but also generates significant compensating force to the ground impact in the initial stance

phase. The two distinct phenomena can be observed in Figure 34; (a) virtual damping creates abrupt high forces at the TD event to deal with ground impact in the impact regions in the figure and (b) the contribution of virtual damping increases as the duration of stance phase decreases and the desired speed increases. As the target locomotion speed increases, the robot's legs experience higher ground impact. Therefore, the effect of the virtual damping becomes significantly higher, which shows the importance of the virtual damping for achieving robustness to the ground impact in locomotion.

6.4.3. Force analysis on the back legs. As shown in Figure 35, forces exerted at the foot-end of the back legs are similarly calculated by using equation (35). As mentioned in Section 5, however, these values are not a good approximation of GRFs because the hip motors are coupled with the spine actuation, which significantly contributes to the generation of different peak forces at foot-end of the front/back legs. Still, the general trends observed in the front legs are similar: (a) contralateral symmetry and (b) higher peak force at higher speeds. To improve tracking/compliance control performance of the back legs, further consideration of the system identification for the spine is required.

7. Concluding remarks and future directions

The MIT Cheetah with the hierarchical controller achieved high speed trot-running using the proprioceptive feedback and the programmable leg-compliance without the robot's body attitude sensory feedback. To achieve highly dynamic locomotion with various gait-patterns, a simple set of parameters was constructed for the controller. The high-level controller consists of the gait-pattern modulator and the leg-trajectory generator, and it allows for the description of the kinematics and kinetics of the robot's running motion. The proprioceptive force-control actuator creates programmable virtual compliance in the robot's

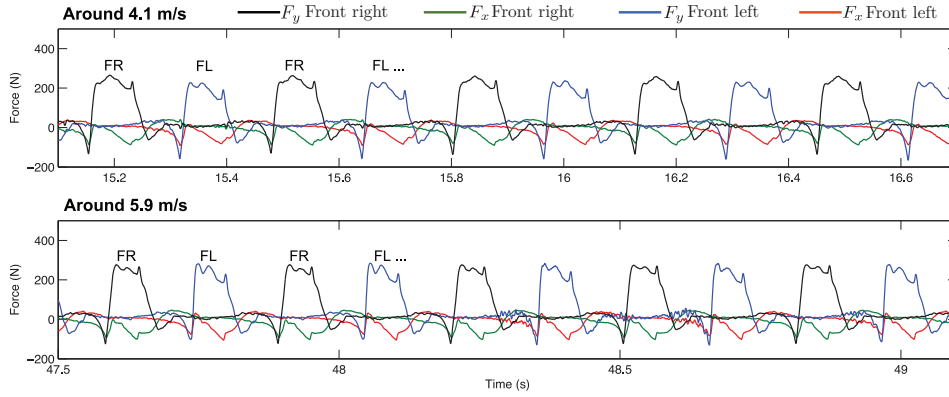


Fig. 33. Estimation of generated forces in Cartesian coordinate at foot-end of front legs. Stance phase (high vertical force region) and swing phase (low vertical force region) can be approximated from the graph. Increase in peak force value is observed with decrease in duty factor.

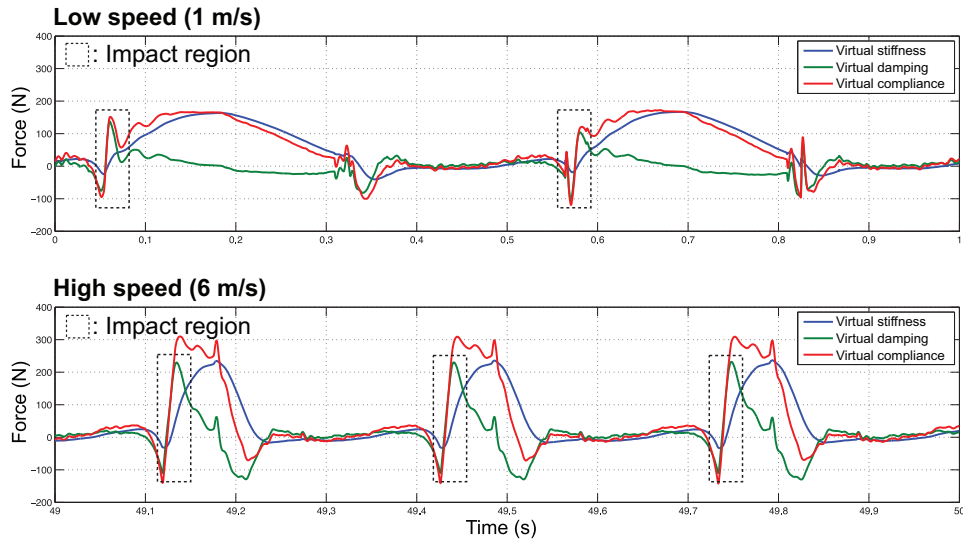


Fig. 34. Contribution of virtual stiffness (5000 N/m) and virtual damping (100 Ns/m) to the creation of the vertical component at the front right foot-end; (top) walking at low speed at 1 m/s; (bottom) high speed at 6 m/s.

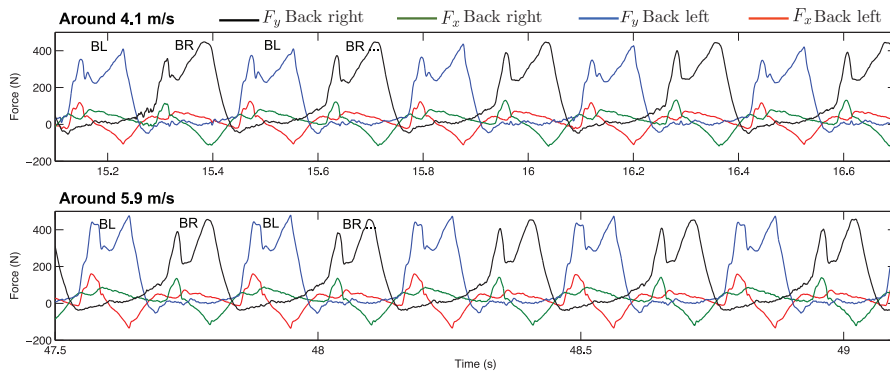


Fig. 35. Estimation of generated forces at foot-end of back legs, in Cartesian coordinates. Increase in peak force value is observed with decrease in duty factor.

leg in the form of low-level individual leg controllers, and enables high bandwidth response to external disturbances, which is important in highly dynamic locomotion. The fast

FPGA/RT control architecture achieved this complicated task without any mechanical springs/dampers installed on the leg, by largely increasing the control loop frequency.

The individual leg controller employs a tunable stance-trajectory design according to the *equilibrium point hypothesis*, as well as a smooth swing-trajectory design by using properties of the Bézier curve. The equilibrium point trajectory for the stance phase is designed by the simple sinusoidal wave, of which amplitude is the control variable in order to adjust the impulses exerted to the ground in the stance phase for running. The virtual compliance and minimal mass/inertia design of the leg actuation system also enabled proprioceptive TD detection without any foot force sensors; based on this event detection, the TD-event based “stride-to-stride” rhythmical gait-pattern modulation is achieved. The MIT Cheetah achieves stable running gait of speed up to 6 m/s ($Fr = 7.34$). This validates self-stabilizing property given from the robot’s leg compliance. Also, a simple gait transition algorithm from trot to gallop at the maximum speed was implemented and tested, and the preliminary results are introduced in this paper. However, in order to achieve a stable gallop or a stable locomotion outside of the treadmill, we need to improve the developed controller as follows:

1. Integrating the robot’s body-attitude sensory feedback with the proposed control framework for field running on rough terrain. To accomplish this, a roll and yaw stabilizing controller will have to be integrated within the present control framework through additional actuators, namely the ab/adduction of each leg. An inertial measurement unit (IMU) sensor is being integrated with the robot to measure its attitude during running.
2. Studying of comparison between the estimated forces and the real GRFs at each foot-end to improve proprioceptive force production/sensing.
3. Identifying the spine system of the robot coupled with back legs to improve performance of the controller. As shown in the experimental results, the effect of the flexible spine coupled with the back legs is not negligible, so that the tracking performance and GRF estimation are deteriorated. The compliant spine will be modeled so that a force compensation for the effect of the spine becomes possible in a feedforward manner. Also, the spine will be actively employed in gallop running.
4. Accomplishing stable gallop for even faster running. With the proposed control framework integrated with the IMU sensor, we expect to achieve gallop gait with a new design of the stance trajectory.

The hierarchical structure of the proposed controller is expected to provide expandability to more complicated intelligent gait algorithms as well as compatibility with low-level force control schemes such as a direct force control with the proprioceptive force control actuator. Extending the proposed control method through these future improvements, we plan to develop a controller that allows galloping in the field.

Acknowledgments

We appreciate the hardware/software support of National Instruments. We owe special thanks to Dr Jooeon Ahn for his advice regarding the stability analysis. We thank Albert Wang, Meng Yee (Michael) Chuah, Shannon Xuan Yang for working with us on the experiment.

Funding

This work was supported by the Defense Advanced Research Program (DARPA) M3 program.

Notes

1. The self-stabilizing means that legged robots can sustain stable dynamic locomotion without sensors on the body dynamics such as body pitch angles and its feedbacks for stabilization.
2. Virtual leg compliance consists of both programmable stiffness and damping on a virtual leg, which is the imaginary line connecting a shoulder/hip to the corresponding foot-end.
3. $SAT(x,y) = \begin{cases} x & \text{if } x \leq y \\ y & \text{Otherwise} \end{cases}$
4. TRACKER 4.82 03 Oct 2013 ©2013 Douglas Brown, www.cabrillo.edu/~dbrown/tracker.
5. Some use different notation, $\frac{v}{\sqrt{gh}}$.
6. At 6 m/s, the total power consumption of the LiPo battery is 973 W and the mechanical power generated from the motors is 234 W.

References

- Alexander RM (1984) The gaits of bipedal and quadrupedal animals. *The International Journal of Robotics Research* 3(2): 49–59.
- Altendorfer R, Koditschek DE and Holmes P (2004) Stability analysis of legged locomotion models by symmetry-factored return maps. *The International Journal of Robotics Research* 23(10–11): 979–999.
- Baraff D (1991) Coping with friction for non-penetrating rigid body simulation. *ACM SIGGRAPH Computer Graphics*, 25(4): 31–41.
- Bares JE and Whittaker WL (1993) Configuration of autonomous walkers for extreme terrain. *The International Journal of Robotics Research* 12(6): 535–559.
- Baumgarte J (1972) Stabilization of constraints and integrals of motion in dynamical systems. *Computer Methods in Applied Mechanics and Engineering* 1(1): 1–16.
- Bizzi E, Hogan N, Mussa-Ivaldi FA, et al. (1992) Does the nervous system use equilibrium-point control to guide single and multiple joint movements? *Behavioral and Brain Sciences* 15(04): 603–613.
- Blickhan R (1989) The spring-mass model for running and hopping. *Journal of Biomechanics* 22(11–12): 1217–1227.
- Blickhan R and Full R (1993) Similarity in multi legged locomotion: Bouncing like a monopode. *Journal of Comparative Physiology A* 173: 509–517.
- Blickhan R, Seyfarth A, Geyer H, et al. (2007) Intelligence by mechanics. *Philosophical Transactions of the Royal Society A: Mathematical, Physical and Engineering Sciences* 365(1850): 199–220.

- Boston Dynamics (2009) Cheetah robot runs 28.3 mph; a bit faster than Usain Bolt. <http://www.youtube.com/watch?v=chPanW0QWhA&feature=youtu.be>.
- Cotton S, Olaru I, Bellman M, et al. (2012) Fastrunner: A fast, efficient and robust bipedal robot. concept and planar simulation. In: *Proceedings of the 2012 IEEE international conference on robotics and automation (ICRA)*, St Paul, MN, USA, 14–18 May 2012, pp. 2358–2364.
- Estremera J and Waldron KJ (2008) Thrust control, stabilization and energetics of a quadruped running robot. *The International Journal of Robotics Research* 27(10): 1135–1151.
- Farley CT, Glasheen J and McMahon TA (1993) Running springs: Speed and animal size. *The Journal of Experimental Biology* 185(1): 71–86.
- Farley CT and Taylor CR (1991) A mechanical trigger for the trot-gallop transition in horses. *Science* 253(5017): 306–308.
- Fukuoka Y, Kimura H and Cohen AH (2003) Adaptive dynamic walking of a quadruped robot on irregular terrain based on biological concepts. *The International Journal of Robotics Research* 22(3–4): 187–202.
- Full RJ and Koditschek DE (1999) Templates and anchors: Neuromechanical hypotheses of legged locomotion on land. *The Journal of Experimental Biology* 202(23): 3325–3332.
- Full RJ, Kubow T, Schmitt J, et al. (2002) Quantifying dynamic stability and maneuverability in legged locomotion. *Integrative and Comparative Biology* 42(1): 149–157.
- Gehring C, Coros S, Hutter M, et al. (2013) Control of dynamic gaits for a quadrupedal robot. In: *Proceedings of the 2013 IEEE international conference on robotics and automation (ICRA)*, Karlsruhe, Germany, 6–10 May 2013, pp. 3287–3292.
- Geyer H, Blickhan R and Seyfarth A (2002) Natural dynamics of spring-like running: Emergence of selfstability. In: *Proceedings of the 5th international conference on climbing and walking robots*, Paris, France, pp. 87–92.
- Ghigliazza R, Altendorfer R, Holmes P, et al. (2003) A simply stabilized running model. *SIAM Journal on Applied Dynamical Systems* 2(2): 187–218.
- Goswami A, Espiau B and Keramane A (1997) Limit cycles in a passive compass gait biped and passivity-mimicking control laws. *Autonomous Robots* 4(3): 273–286.
- Grillner S and Wallen P (1985) Central pattern generators for locomotion, with special reference to vertebrates. *Annual Review of Neuroscience* 8(1): 233–261.
- Gross M, Rummel J and Seyfarth A (2009) Stability in trotting dogs. In: *Proceedings of the international symposium on adaptive motion in man, animals, and machines*, Jena, Germany, 19–20 February 2009.
- Haberland M, KarsSEN JGD, Kim S, et al. (2011) The effect of swing leg retraction on running energy efficiency. In: *Proceedings of the 2011 IEEE/RSJ international conference on intelligent robots and systems (IROS)*, San Francisco, CA, USA, 25–30 September 2011, pp. 3957–3962.
- Hodgins JK and Raibert M (1991) Adjusting step length for rough terrain locomotion. *IEEE Transactions on Robotics and Automation* 7(3): 289–298.
- Hogan N (1985) Impedance control—An approach to manipulation. I. Theory. II. Implementation. III. Applications. *ASME Transactions Journal of Dynamic Systems and Measurement Control B* 107: 1–24.
- Hogan N (1987) Stable execution of contact tasks using impedance control. In: *Proceedings of the IEEE international conference on robotics and automation*, Raleigh, NC, March 1987, Vol. 4, pp. 1047–1054.
- Hurmuzlu Yildirim and Marghitu DB (1994) Rigid body collisions of planar kinematic chains with multiple contact points. *The International Journal of Robotics Research* 13(1): 82–92.
- Ijspeert AJ (2008) Central pattern generators for locomotion control in animals and robots: a review. *Neural Networks* 21(4): 642–653.
- Jung S, Hsia T and Bonitz R (2004) Force tracking impedance control of robot manipulators under unknown environment. *IEEE Transactions on Control Systems Technology* 12(3): 474–483.
- Kalakrishnan M, Buchli J, Pastor P, et al. (2011) Learning, planning, and control for quadruped locomotion over challenging terrain. *The International Journal of Robotics Research* 30(2): 236–258.
- Kim S, Clark JE and Cutkosky MR (2006) isprawl: Design and turning for high-speed autonomous open-loop running. *The International Journal of Robotics Research* 25: 903–912.
- Koepl D and Hurst J (2011) Force control for planar spring-mass running. In: *Proceedings of the 2011 IEEE/RSJ international conference on intelligent robots and systems (IROS)*, San Francisco, CA, USA, 25–30 September 2011, pp. 3758–3763.
- Koepl D, Kemper K and Hurst J (2010) Force control for spring-mass walking and running. In: *Proceedings of the IEEE/ASME international conference on advanced intelligent mechatronics (AIM)*, Montreal, Canada, pp. 639–644.
- Kolter JZ, Rodgers MP and Ng AY (2008) A control architecture for quadruped locomotion over rough terrain. In: *Proceedings of the IEEE international conference on robotics and automation (ICRA)*, Pasadena, CA, USA, 19–23 May 2008, pp. 811–818.
- Krasny DP and Orin DE (2010) Evolution of a 3D gallop in a quadrupedal model with biological characteristics. *Journal of Intelligent and Robotic Systems* 60(1): 59–82.
- Kubow T and Full R (1999) The role of the mechanical system in control: a hypothesis of self-stabilization in hexapedal runners. *Philosophical Transactions of the Royal Society of London. Series B: Biological Sciences* 354(1385): 849–861.
- Lee DV, Bertram JE and Todhunter RJ (1999) Acceleration and balance in trotting dogs. *The Journal of Experimental Biology* 202(24): 3565–3573.
- Lee J (2013) *Hierarchical controller for highly dynamic locomotion utilizing pattern modulation and impedance control: Implementation on the MIT Cheetah robot*. Master's Thesis, Department of Mechanical Engineering, MIT, Cambridge, MA.
- Maes LD, Herbin M, Hacker R, Bels VL and Abourachid A (2008) Steady locomotion in dogs: Temporal and associated spatial coordination patterns and the effect of speed. *The Journal of Experimental Biology* 211: 138–149.
- Maufroy C, Kimura H and Takase K (2010) Integration of posture and rhythmic motion controls in quadrupedal dynamic walking using phase modulations based on leg loading/unloading. *Autonomous Robots* 28(3): 331–353.
- McGeer T (1990) Passive dynamic walking. *The International Journal of Robotics Research* 9(2): 62–82.
- McGhee RB and Frank AA (1968) On the stability properties of quadruped creeping gaits. *Mathematical Biosciences* 3: 331–351.

- McMahon TA, Valiant G and Frederick EC (1987) Groucho running. *Journal of Applied Physiology* 62(6): 2326–2337.
- Poulakakis I, Papadopoulos E and Buehler M (2006) On the stability of the passive dynamics of quadrupedal running with a bounding gait. *The International Journal of Robotics Research* 25: 669–687.
- Raiert M, Blankespoor K, Nelson G, et al. (2008) Bigdog, the rough-terrain quadruped robot. In: *Proceedings of the 17th world congress the international federation of automatic control (IFAC)*, Seoul, South Korea, 6–11 July 2008, pp. 10822–10825.
- Remy CD (2011) *Optimal exploitation of natural dynamics in legged locomotion*. PhD Thesis, ETH, Zurich.
- Righetti L and Ijspeert AJ (2008) Pattern generators with sensory feedback for the control of quadruped locomotion. In: *Proceedings of the IEEE international conference on robotics and automation (ICRA)*, Pasadena, CA, USA, 19–23 May 2008, pp. 819–824.
- Ringrose R (1997) Self-stabilizing running. In: *Proceedings of the IEEE international conference on robotics and automation*, Roma, Italy, 10–14 April 2007, Vol. 1, pp. 487–493.
- Seipel J and Holmes P (2007) A simple model for clock-actuated legged locomotion. *Regular and Chaotic Dynamics* 12(5): 502–520.
- Seok S, Wang A, Chuah MY, et al. (2013) Design principles for highly efficient quadrupeds and implementation on the MIT cheetah robot. In: *Proceedings of the IEEE international conference on robotics and automation (ICRA)*, Karlsruhe, Germany, 6–10 May 2013, pp. 3292–3297.
- Seok S, Wang A, Otten D, et al. (2012) Actuator design for high force proprioceptive control in fast legged locomotion. In: *Proceedings of the IEEE/RSJ international conference on intelligent robots and systems (IROS)*, San Francisco, CA, USA, 25–30 September 2011, pp. 1970–1975.
- Shkolnik A, Levashov M, Manchester IR, et al. (2011) Bounding on rough terrain with the littledog robot. *The International Journal of Robotics Research* 30(2): 192–215.
- Spröwitz A, Tuleu A, Vespignani M, et al. (2013) Towards dynamic trot gait locomotion: Design, control, and experiments with Cheetah-Cub, a compliant quadruped robot. *The International Journal of Robotics Research* 32(8): 1–19.
- Tucker VA (1975) The energetic cost of moving about: Walking and running are extremely inefficient forms of locomotion. Much greater efficiency is achieved by birds, fish—and bicyclists. *American Scientist* 63(4): 413–419.
- Vilensky JA, Libii JN and Moore AM (1991) Trot–gallop gait transitions in quadrupeds. *Physiology and Behavior* 50: 835–842.
- Walter RM and Carrier DR (2006) Ground forces applied by galloping dogs. *The Journal of Experimental Biology* 210: 208–216.
- Wickler SJ, Hoyt DF, Cogger EA, et al. (2003) The energetics of the trot–gallop transition. *The Journal of Experimental Biology* 206(9): 1557–1564.
- Witkin A, Gleicher M and Welch W (1990) Interactive dynamics. In: *I3D '90 proceedings of the 1990 symposium on interactive 3D graphics*, pp. 11–21. New York: ACM.
- Yoneda K, Iiyama H and Hirose S (1994) Sky-hook suspension control of a quadruped walking vehicle. In: *Proceedings of the IEEE international conference on robotics and automation (ICRA)*, San Diego, CA, USA 8–13 May 1994, pp. 999–1004.

Appendix A: Index to Multimedia Extension

The multimedia extension page is found at <http://www.ijrr.org>

Table of Multimedia Extension

Extension	Media type	Description
1	Video	I. Gait pattern generator II. Leg trajectory generator III. Virtual leg compliance IV. Proprioceptive touch-down feedback V. MIT Cheetah simulator VI. Gait test in the air VII. MIT Cheetah running on the treadmill VIII. Gait transition IX. Torque vs angular velocity at each joint

Appendix B: Model parameters

Table 6 shows the model parameters of the MIT Cheetah depicted in Figure 36.

Table 6. Model parameters.

Segment	Mass (kg)	Moi ^a (kgm ²)	Length (m)
Body _F	4.84	0.300	0.200
Scapula _F ^b	2.63	0.00829	0.160
Humerus _F	0.160	0.00237	0.220
Radius _F	0.120	0.00123	0.222
Spine segment	0.0562	0.0000682	0.0360
Body _B	1.92	0.282	0.187
Femur _B ^b	2.70	0.0163	0.245
Tibia _B	0.160	0.00237	0.220
Metatarsals _B	0.0850	0.000558	0.165
Stator of the electric actuator	2.61	0.00717	—

^aMoment of inertia.

^bIncluding the rotor mass/inertia of the electric motor.

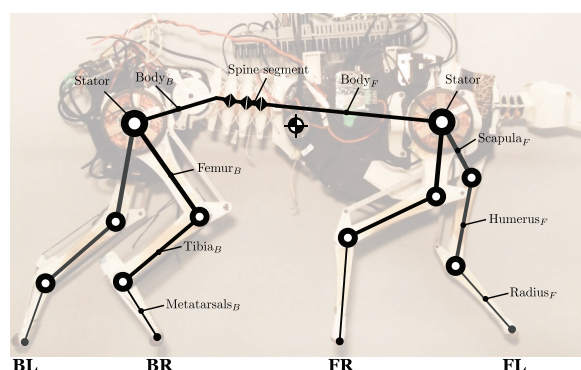


Fig. 36. Terminology for MIT Cheetah model.

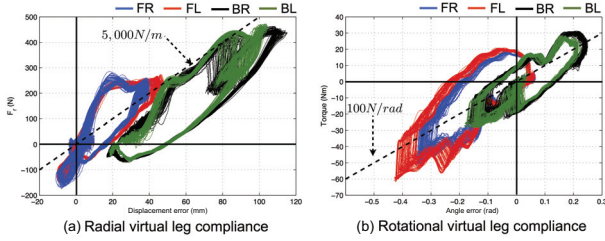


Fig. 37. The robot's virtual leg compliance in the polar coordinate (r, θ): (a) radial virtual stiffness 5000 N/m with virtual damping 100 Ns/m; (b) angular virtual stiffness 100 N/rad with virtual damping 4 Ns/rad.

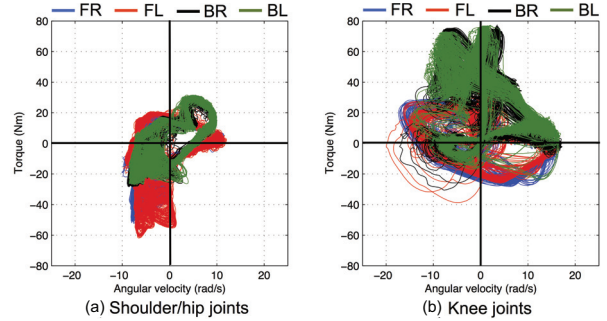


Fig. 38. Torque vs. angular velocity curves for shoulder/hip and knee joints while trotting in $\sim 1\text{--}6$ m/s during the experiment.

Appendix C: Spine coordination

The four joints of the spine

$$q_{\text{spine}} = C_s(q_{\text{humerus,BL}} + q_{\text{humerus, BR}}) \quad (36)$$

$$q_{\text{backpitch}} = q_{\text{frontpitch}} + 4q_{\text{spine}} \quad (37)$$

where $C_s = \frac{393}{6400}$ is the effective differential gear ratio.

Appendix D: Properties of derivatives of the Bézier curve

A r th derivative of a Bézier curve is formulated as below and therefore it has the following useful properties:

$$p_i^{(r)}(s) = \frac{n!}{(n-r)!} \sum_{k=0}^{n-r} \Delta^r c_k B_k^{n-r}(s) \quad (38)$$

- $p_i^{\text{SW}}|_{S_i^{\text{SW}}=0} = c_0$ $v_i^{\text{SW}}|_{S_i^{\text{SW}}=0} = n\Delta c_0/\hat{T}_{\text{sw}}$;
- $p_i^{\text{SW}}|_{S_i^{\text{SW}}=1} = c_n$ $v_i^{\text{SW}}|_{S_i^{\text{SW}}=1} = n\Delta c_n/\hat{T}_{\text{sw}}$;
- double-overlapped control points generate zero velocity;
- triple-overlapped control points generate zero acceleration.

Δ^r is r th forward difference operator: $\Delta^r c_k = \Delta^{r-1} c_{k+1} - \Delta^{r-1} c_k$.

Appendix E: Virtual leg compliance

During the experiment, the virtual leg compliance created in the impedance control manner is shown in (a) the force vs radial position error plot and (b) the torque vs angular position error plot for each leg in Figure 37. The virtual damping induces the virtual compliance curve to deviate

away from the virtual pure stiffness line (straight line) while providing reflex response to ground impact.

Appendix F: Joint actuator requirement

For the dual-coaxial actuator of the MIT Cheetah, a commercial motor (Emoteq HT-5001, torque constant of 0.27 Nm/A, weight: 1.3 kg, phase resistance: 0.354 Ω , peak torque: 10 Nm) was integrated with a planetary gear set (gear ratio: 5.8 : 1). The 2-DoF leg system is actuated by the dual coaxial motor unit through the pantographic leg design. Torque vs angular velocity curves at each joint during the experiment are drawn together in Figure 38. The values of torque are calculated from the measured applied current by the current sensor in the motor driver and the kinematic data from the encoders for each joint. The values of angular velocity are also derived from the positional data from the encoders. These plots indicate the requirement of the actuation specification for the robot's leg joints in the running experiment. Therefore, with these plots, various set of actuators can be developed.

Appendix G: Gait transitioning

The additional experiment was executed with the expanded hierarchical controller integrated with the IMU sensor. The flexible spine was replaced with the rigid spine. The proposed method for the gait transition by linearly changing the phase differences during 2.5 s was exactly applied.

As shown in Figure 39, periodic stable trotting and galloping before/after the trot-to-gallop transition were achieved on the treadmill with the speed of 3.2 m/s, which implies that the proposed gait transition method was effective. A following paper will address the details about how to achieve a stable gallop.

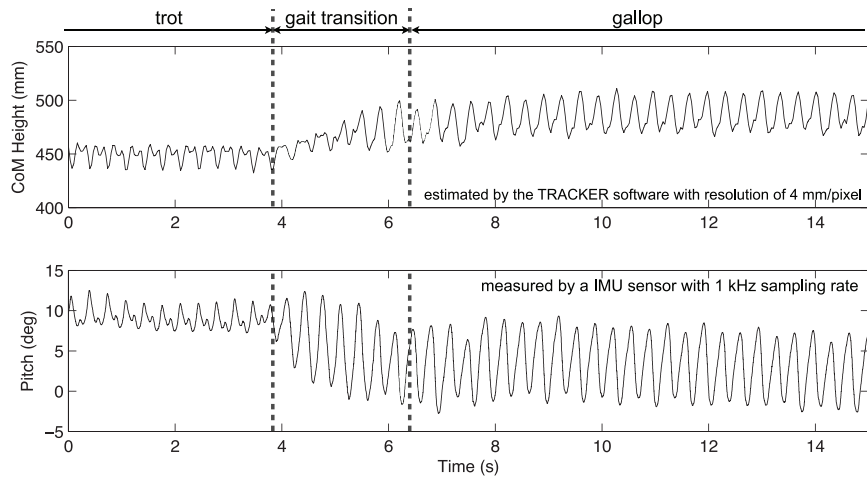


Fig. 39. Height of COM (mm) and pitch (deg) variation in the 2.5 s trot-to-gallop gait transition of the MIT Cheetah on the treadmill with a speed of 3.2 m/s; the IMU sensor was used to get pitch data and the tracker software for the motion capture on a gallop video was used to get height data.